Magnetic Order and Spin Reorientations of RGa (R = Gd, Dy, Ho and Er) Intermetallic Compounds

by

Resta Susilo

A Thesis submitted to the Faculty of Graduate Studies of

The University of Manitoba

in partial fulfilment of the requirements of the degree of

MASTER OF SCIENCE

Department of Physics and Astronomy

University of Manitoba

Winnipeg

Abstract

The magnetic structures and spin reorientations of RGa (R = Gd, Dy, Ho and Er) intermetallic compounds have been investigated using neutron powder diffraction and rare earth Mössbauer spectroscopy. The aim has been to determine the magnetic structures of these compounds before and after their spin reorientation transitions and to understand the role of the crystal field and exchange interactions in the spin reorientation mechanism. The results have been compared with those found from previous single-crystal susceptibility measurements on RGa and the recent ^{119}Sn Mössbauer spectroscopy work on Sn-doped RGa compounds. The magnetic structures obtained at low temperatures are a simple collinear ferromagnetic in DyGa, canted ferromagnetic in HoGa and a non-collinear ferromagnetic in GdGa. The spin reorientation in ErGa was also observed by ^{166}Er Mössbauer spectroscopy. These results show that both the crystal field and exchange interactions play an important role in the reorientation mechanism.

Acknowledgements

I would like to thank all people who have helped and supported me in preparing this thesis. Firstly I owe enormous thanks to my supervisor Professor Sean Cadogan for all of his help, advice and the fruitful discussions during the work on this thesis. I also learnt a huge amount from Dr. Susset Muñoz-Pérez, Dr. Raiden Cobas Acosta and Dr. Pierric Lemoine with whom I have collaborated closely throughout this work.

I would like to thank Professor Dominic Ryan (McGill University) for neutron diffraction patterns of GdGa, ^{155}Gd and ^{166}Er Mössbauer spectra, and for many useful discussions. I would also like to thank Nicholas Lee-Hone (McGill University) for his fitting work on ^{166}Er Mössbauer spectra.

I am very grateful for the good friends I made during my time at the U of M and also for Mrs. Chooi, Bob and my housemates for making me feel at home. I would like to thank my family, especially my parents for their understanding and moral supports that enabled me to start and finish this work. Last but not least, I would like to thank Nopianti for the chocolates many years ago and everything since.

For my parents

Table of Contents

List of Tables

List of Figures

List of Copyrighted Materials

1. Introduction

1.1. Background

Rare-earth intermetallic compounds are now engaging the attention of large numbers of physicists, chemists, material scientists and engineers, for such compounds are important from both the fundamental and technological points of view. Fundamentally, the rare-earth intermetallic compounds show a great range and diversity in their structures and stoichiometries, which in some cases show unique magnetic behaviour, complex magnetic structures, a wide range of crystal field effects, and so on. From the technological point of view, rare-earth intermetallic compounds are the basis of the world's strongest permanent magnets and are also the subject of much recent interest as potential magnetic refrigerant materials.

Research on rare earth intermetallic compounds is mainly focused on the compounds of rare earth (R) and transition metals (T), due to their application as permanent magnets. In contrast, intermetallic compounds of rare earth and non- magnetic metals, especially the group IIIA elements (e.g. B, Al, and Ga), have received less attention (Wallace 1973). RAl_2, RB_4, RB_6 and RGa_2 are the only compounds of rare earth and group IIIA elements that have been the subject of significant investigations over the past decades. RAl_2 compounds have attracted most of the attention among all the rare earth-aluminum compounds for their complex magnetic behaviour, particularly because one needs to consider crystal field effects in order to get a consistent description of their behaviour (Buschow 1979). RB_4 compounds have a wide variety of both interesting structural and physical properties such as magnetic phase transitions, heavy fermion

behaviour, mixed valence phenomena and superconductivity (Gignoux & Schmitt 1997). RB_6 compounds have attracted some investigations due to the valence instabilities and k-f hybridization phenomena which produce unusual magnetic properties in these compounds (Gignoux & Schmitt 1997). RGa_2 compounds have been investigated extensively, due to their complex magnetic phase diagrams which show the occurrence of commensurate and incommensurate magnetic structures as a function of temperature (Gignoux & Schmitt 1997). Recent studies of the magnetocaloric properties of RGa_2 compounds (Reis et al. 2010) show that these compounds have similar magnetocaloric properties as the RCo_2 compounds which is one candidate system for magnetic refrigerant applications.

Several recent reports have appeared regarding the magnetocaloric effect in the RGa (R = Gd, Ho and Er) intermetallic compounds, showing the potential of these compounds as magnetic refrigerant materials (Chen et al. 2009, Zhang et al. 2009, Chen et al. 2010). It was found that these compounds have a large reversible magnetocaloric effect and a giant value of the refrigerant capacity (RC) which is related to the two magnetic transitions: the transition from paramagnetic to ferromagnetic and the spin reorientation transition. The occurrence of a spin reorientation in these compounds is interesting from the fundamental magnetism point of view, because the competition between the crystal field and exchange interactions might play an important role in the reorientation mechanism.

Given the interesting magnetic behaviour and the possibility that the crystal field interaction might induce the spin reorientation in these compounds, we felt that more detailed investigations using neutron diffraction and rare earth Mössbauer spectroscopy

were needed, with particular emphasis on those RGa compounds with heavy rare earth elements (GdGa, DyGa, HoGa and ErGa). In the following sections, the previous work on RGa intermetallic compounds will be discussed. In section 1.2, we will discuss the crystal structure and the magnetic properties of the RGa compounds, and finally in Section 1.3, the magnetic structure and spin reorientation determinations using ^{119}Sn Mössbauer spectroscopy on Sn-doped RGa intermetallic compounds (Delyagin et al. 2007) will be discussed briefly.

1.2. Crystal structure and magnetic properties of RGa intermetallic compounds

Equiatomic compounds of rare earth and gallium (RGa) with the CrB-type structure were first prepared in the early 1960's (Baenziger & Moriarty 1961, Cable et al. 1964). Dwight et al. (1967) then extended the study to determine whether all RGa compounds were isostructural. They found that all RGa intermetallic compounds adopt the orthorhombic CrB-type structure (*Cmcm* space group). Both the rare earth and gallium occupy 4c sites with the *m2m* point symmetry and the atomic positions (0, y, ¼), (0, –y, ¾), (½, ½+y, ¼) and (½, ½-y, ¾). The structure itself can be viewed as the stacking of trigonal prisms along the crystallographic a-axis with rare earth atoms at the corners and the gallium atoms nearly at the centers (Baenziger & Moriarty 1961), as shown in Figure 1.1. The lattice constants of the RGa (R = Pr – Er) compounds at room temperature are summarized in Table 1.1.

Cable et al. (1964) determined the magnetic structure of TbGa using neutron diffraction. They reported that TbGa is a collinear ferromagnet with a Curie temperature

of 155 K. In their calculations of the magnetic scattering intensities, they assumed that the Tb moment is 9 μ_B, and they found that the Tb magnetic moments are oriented along the crystallographic c-axis at 77 K.

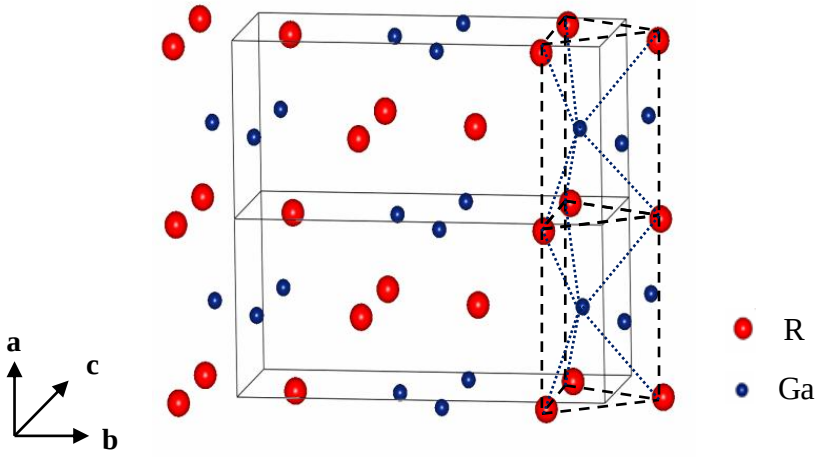

Figure 1.1. Crystal structure of the RGa compounds.

Barbara et al. (1971) reported the magnetic properties and magnetic structures of both TbGa and ErGa. They performed magnetic measurements on a single-crystal of TbGa in fields up to 80 kOe and they showed that TbGa is ferromagnetic with the easy direction of magnetization being the c-axis, in agreement with Cable et al. (1964). A large hysteresis in both the paramagnetic and ferromagnetic regimes was also observed. Neutron diffraction measurements carried out at 4.2 K and 300 K (for ErGa) and at 4.2 K, 77 K and 300 K (for TbGa) reveal that at 4.2 K the magnetic structures of ErGa and TbGa are both non-collinear ferromagnets. They described the magnetic structure of ErGa as a coexistence of ferromagnetic order along the crystallographic a-axis and antiferromagnetic order along the b-axis, as shown in Figure 1.2.

The magnetic properties of the RGa (R = Pr - Er) compounds were reported by Fujii et al. (1971), based on magnetization and susceptibility measurements on polycrystalline samples in fields up to 16 kOe from 4.2 to 400 K. They showed that all RGa compounds are ferromagnetic. The magnetization values were reported to be smaller in magnitude than the theoretical saturation moments of the R^{3+} ions which indicates that the external field of 16 kOe was insufficient to saturate the magnetization due to the large magnetocrystalline anisotropy in the RGa compounds.

Table 1.1. The lattice parameters of the RGa compounds (Dwight et al. 1967).

Compound	**a (Å)**	**b (Å)**	**c (Å)**
CeGa	4.4651(3)	11.4248(7)	4.2153(2)
PrGa	4.4410(1)	11.3370(3)	4.1992(1)
NdGa	4.4164(2)	11.2758(6)	4.1835(2)
SmGa	4.3806(1)	11.1219(3)	4.1471(1)
GdGa	4.3372(3)	11.0316(8)	4.1106(3)
TbGa	4.3114(2)	10.9394(5)	4.0851(2)
DyGa	4.2913(11)	10.8740(29)	4.0672(11)
HoGa	4.2740(7)	10.8008(19)	4.0501(7)
ErGa	4.2523(9)	10.7443(23)	4.0329(9)
TmGa	4.2371(7)	10.6882(18)	4.0218(7)
LuGa	4.2090(5)	10.5817(13)	4.0001(5)

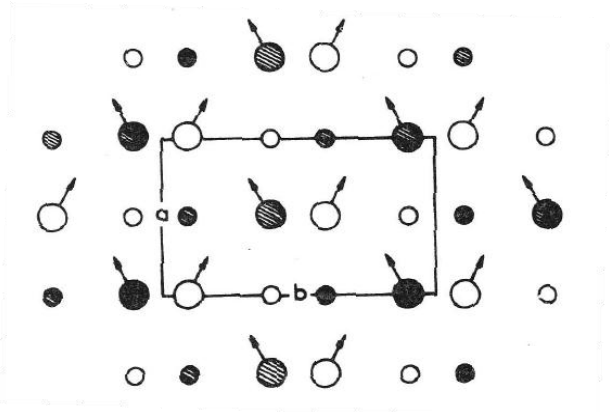

Figure 1.2. Schematic arrangement of the Er moments in ErGa at 4.2 K (Barbara et al. 1971). Large and small circles indicate the Er and Ga atoms. The hatched and empty circles represent atoms at z = 0.75 and z = 0.25, respectively.

In 1974, Iraldi et al. carried out ^{161}Dy Mössbauer spectroscopy on DyGa (Iraldi et al. 1974). They found similar quadrupole interaction and hyperfine field values between pure Dy metal and DyGa, indicating that the ground state of the Dy^{3+} ion in DyGa is nearly a $\left|\pm\frac{15}{2}\right\rangle$ doublet. From the hyperfine field data, they were able to deduce a Dy moment of 9.8 μ_B.

The work carried out by Fujii et al. (1971) was extended by Shohata et al. (1974) and Shohata (1977) with magnetization and susceptibility measurements on single-crystal RGa (R = Pr – Er) compounds. The magnetic properties of the RGa compounds are summarized in Table 1.2. Shohata et al. found that DyGa, TbGa and HoGa are simple ferromagnets with the easy magnetization direction along the c-axis. TbGa and DyGa were found to exhibit large hysteresis along their easy magnetization direction which might be a consequence of the intrinsic domain wall freezing associated with a large anisotropy energy. Magnetization measurements on single-crystal ErGa reveal that the easy direction of magnetization is the b-axis. Shohata et al. noted that the saturation moment of Er along the b-axis is smaller than the theoretical value of 9 μ_B for the Er^{3+} ion, which could indicate a non-collinear magnetic structure in ErGa. They also found a sudden increase in magnetization along the a-axis at about 5 kOe as shown in Figure 1.3, which they assumed to be caused by a spin flip of the Er^{3+} moments. From the magnetization curves, the saturation values of the R moments in PrGa, NdGa and SmGa were found to be smaller than the theoretical 'free-ion' values. This reduction in moment may originate from a partial quenching of the R^{3+} magnetic moment in each compound by the crystal field. The paramagnetic susceptibilities of SmGa did not obey the Curie-Weiss law. This behaviour can be interpreted in terms of Van Vleck theory as the

admixture of higher energy J multiplets into the ground state. They were also able to deduce the second-order diagonal and off-diagonal crystal field parameters B_{20} and B_{22} from the paramagnetic Curie temperature based on the molecular field theory (equation (2.16)) as listed in Table 1.3. However, it should be noted that the above cited authors were unable to describe the magnetic properties of GdGa.

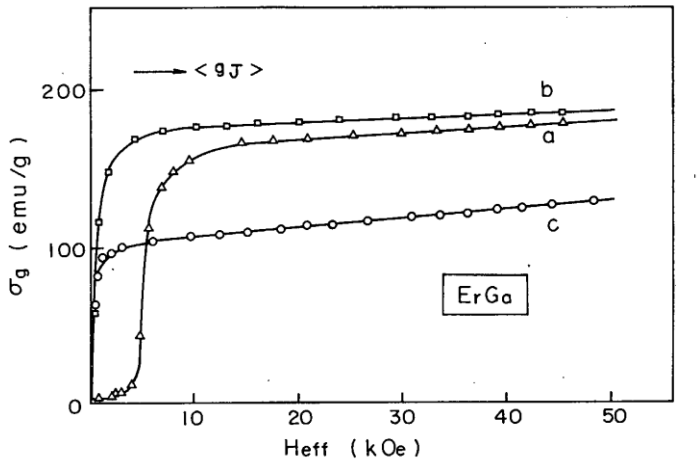

Figure 1.3. Magnetization curves of ErGa at 4.2 K (Shohata 1977)

Table 1.2. The Curie temperature, paramagnetic Curie temperature (θ_p), and paramagnetic Curie temperatures along the a, b and c-axes (θ_a, θ_b and θ_c respectively) of single-crystal RGa compounds. (Shohata 1977)

Compound	**T_c (K)**	**θ_p (K)**	**θ_a (K)**	**θ_b (K)**	**θ_c (K)**
PrGa	32	18	28	8	46
NdGa	44	30	41	34	43
SmGa	108	-	-	-	-
GdGa	183	199	-	-	-
TbGa	158	161	134	134	175
DyGa	116	119	94	68	133
HoGa	63	53	53	42*	68
ErGa	32	26	35	35	12

* erroneously written as 22 K in the original paper

Table 1.3. The crystal field parameters of the RGa compounds (Shohata 1977)

	B_{20} (K)*	B_{22} (K)*
PrGa	1.23	-1.16
NdGa	0.28	-0.10
TbGa	0.41	-1.23
DyGa	0.61	-0.80
HoGa	0.21	-0.26
ErGa	-0.15	0.46

* all values have been converted to SI units from the original paper

1.3. Spin reorientation in RGa intermetallic compounds – ^{119}Sn Mössbauer study on Sn-doped RGa compounds

Nesterov et al. (1992) reported spin reorientation transitions in NdGa, HoGa and ErGa upon cooling below the Curie temperature. This work was extended by Delyagin et al. (2007) based on ^{119}Sn Mössbauer spectroscopy on Sn-doped RGa compounds. The Sn dopant (which occupies the Ga sites) is non-magnetic thus any hyperfine field at this site is transferred from the neighbouring magnetic order of the R sublattice. Information about the ordering direction can be deduced by determining the orientation of the hyperfine field within the principal axis frame of the Electric Field Gradient (EFG) at the ^{119}Sn site. Therefore, the ^{119}Sn Mössbauer spectra will reflect the magnetic structure of the RGa compounds.

Delyagin et al. observed that all spectra can be fitted with a single magnetic sub-spectrum for ^{119}Sn impurity atoms at the Ga site, except the spectrum of GdGa (Figure

1.4). For GdGa, two magnetic subspectra of equal intensity were needed to fit the spectrum below the spin reorientation transition (~110 K) which suggests the existence of a non-collinear magnetic structure in GdGa at low temperatures. It was also observed that this non-collinear structure becomes collinear above the spin reorientation temperature. In addition, spin reorientations were observed in SmGa, NdGa, HoGa and ErGa, consistent with the previous findings of Nesterov et al. (1992). Delyagin et al. showed that the above-mentioned compounds undergo spin reorientations from the bc-plane to the a-axis, although in their paper they were only able to resolve the canting angle of the Ho and Nd moments in HoGa and NdGa as a function of temperature below the spin reorientation transition. However, they commented that their result was insensitive to the azimuthal angle defining the direction of the R moments.

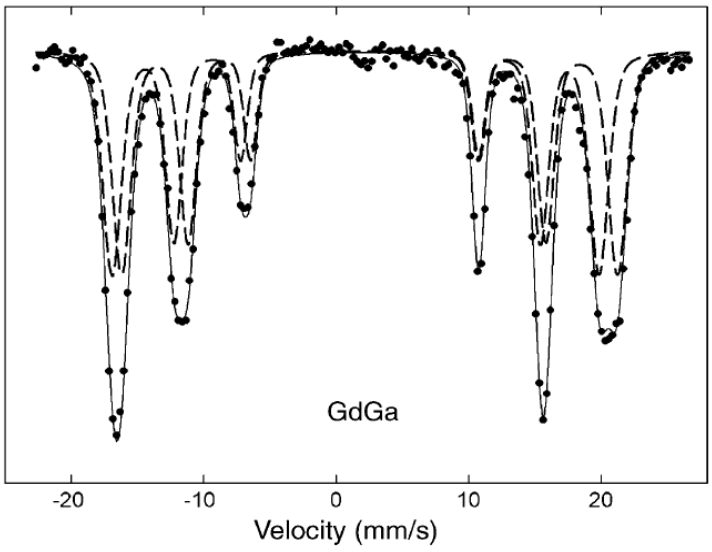

Figure 1.4. ^{119}Sn Mössbauer spectrum for Sn atoms in Ga sites in GdGa at 5 K. The spectrum is well fitted using two magnetic subspectra indicated by the dashed curves. (Delyagin et al. 2007)

From the hyperfine field data, they concluded that these compounds only have two possible orientations of the magnetic moments at temperatures between the spin reorientation and Curie temperatures, namely the crystallographic b and c-axes. They argued that the spin reorientations in the RGa compounds are due primarily to the competition between the exchange interaction and the crystal field effects. The spin reorientation transitions do not occur in PrGa, TbGa and DyGa which have the largest value of the electric quadrupole moment, defined as $Q_{4f} = \frac{1}{2}\alpha_J(3{J_z}^2 - J(J+1))$ (Delyagin et al. (2007)), hence the crystal field interactions dominate the exchange interactions in these compounds.

1.4. Summary

In this chapter we have reviewed the previous work on the crystallography, magnetic properties and magnetic structures of the RGa intermetallic compounds, concentrating on the magnetic anisotropy and the occurrence of spin reorientations in these compounds. It was shown that the RGa compounds possess large magnetocrystalline anisotropy. ErGa shows a unique magnetic behaviour which might indicate the occurrence of a non-collinear spin structure at low temperatures. Based on ^{119}Sn Mössbauer spectroscopy, the magnetic structure of GdGa is a non-collinear ferromagnet below the spin reorientation temperature. The Ho moments were also found to be canted away from the bc-plane to the a-axis upon cooling below the spin reorientation temperature.

2. Theoretical Background

2.1. Magnetic Neutron Scattering

Neutron scattering has become one of the most powerful techniques for microscopic condensed matter studies due to the unique properties of the neutron (Squires 1978, Rossat-Mignod 1987, Chatterji 2006). One of its important properties is that the neutron has a magnetic moment (spin ½), so it can interact with the unpaired electrons in a magnetic atom. Inelastically, this interaction provides information about the magnetic excitation energies. Elastic neutron scattering, which will be used intensively in this work, gives information about the magnetic structure of the scattering system.

In this section, the general formulation of the neutron scattering cross section from a magnetic material and a simple method for determining the direction of the magnetic moments in a ferromagnet will be discussed briefly. Readers should refer to Squires (1978) and Rossat-Mignod (1987) for more detailed derivations.

In a neutron scattering experiment, the counting rate C in a detector that makes a solid angle $d\Omega$ and has an efficiency ζ is given by (Rossat-Mignod 1987)

$$C = \phi \, d\Omega \, \zeta \left(\frac{d\sigma}{d\Omega}\right) \tag{2.1}$$

where ϕ is the flux of the incoming neutron beam and $\left(\frac{d\sigma}{d\Omega}\right)$ is the number of neutrons scattered per second into a solid angle $d\Omega$ which is known as the differential cross section. From the above equation, only the $\left(\frac{d\sigma}{d\Omega}\right)$ term is actually measured in a scattering experiment and it contains information about the scattering system. Therefore, in the following discussion we will focus on this term only and the mathematical expressions

relevant to neutron scattering experiments on a magnetic material.

Suppose our scattering system is a magnetic crystal. For an unpolarized incoming neutron beam, there will be no interference between the nuclear and magnetic scattering (Rossat-Mignod 1987), thus the total differential section can be written as

$$\left(\frac{d\sigma}{d\Omega}\right)(\vec{\boldsymbol{Q}}) = \left(\frac{d\sigma_N}{d\Omega}\right)(\vec{\boldsymbol{Q}}) + \left(\frac{d\sigma_M}{d\Omega}\right)(\vec{\boldsymbol{Q}}) \tag{2.2}$$

where $\left(\frac{d\sigma_N}{d\Omega}\right)(\vec{\boldsymbol{Q}})$and $\left(\frac{d\sigma_M}{d\Omega}\right)(\vec{\boldsymbol{Q}})$ are the elastic nuclear and magnetic cross sections, respectively. The elastic nuclear cross section is usually written as

$$\left(\frac{d\sigma_N}{d\Omega}\right)(\vec{\boldsymbol{Q}}) = N\frac{(2\pi)^3}{v_o}\sum_{\tau}\left|F_N(\vec{\boldsymbol{Q}})\right|^2\delta(\vec{\boldsymbol{Q}}-\vec{\boldsymbol{\tau}}) \tag{2.3}$$

where N is the total number of atoms in the unit cell, and v_o is the volume of the unit cell. The $\delta(\vec{\boldsymbol{Q}}-\vec{\boldsymbol{\tau}})$ term is actually the nuclear Bragg relation, i.e. Bragg scattering only occurs when the scattering vector $\vec{\boldsymbol{Q}} = \overrightarrow{k_i} - \overrightarrow{k_f}$ equals the reciprocal lattice vector $\vec{\boldsymbol{\tau}}$**.** Figure 2.1 illustrates the elastic condition for diffraction in reciprocal space. Bragg scattering only occurs when a reciprocal lattice point lies on the surface of the Ewald Sphere of radius $\left|\overrightarrow{k_i}\right| = \left|\overrightarrow{k_f}\right| = \frac{2\pi}{\lambda}$. Moreover, in equation (2.3)**,** $F_N(\vec{\boldsymbol{Q}})$ is the nuclear structure factor and is given by

$$F_N(\vec{\boldsymbol{Q}}) = \sum_r \overline{b_r}\exp(i\vec{\boldsymbol{Q}}\cdot\vec{\boldsymbol{r}})\exp(-2W) \tag{2.4}$$

where b_r is the scattering length of the atom *r*. The scattering length itself is a complex number. There are two types of nuclei based on their scattering length. First, those nuclei that have a large imaginary component of the scattering length which varies rapidly with the energy of the neutron. Since the imaginary part corresponds to neutron absorption, such nuclei strongly absorb incoming neutrons. Second are those nuclei that have a small

imaginary component of the scattering length and the scattering length is effectively independent of the energy of the neutron. The $\exp(-2W)$ term is the Debye-Waller factor which represents the thermal vibration of the scattering atoms about their equilibrium positions.

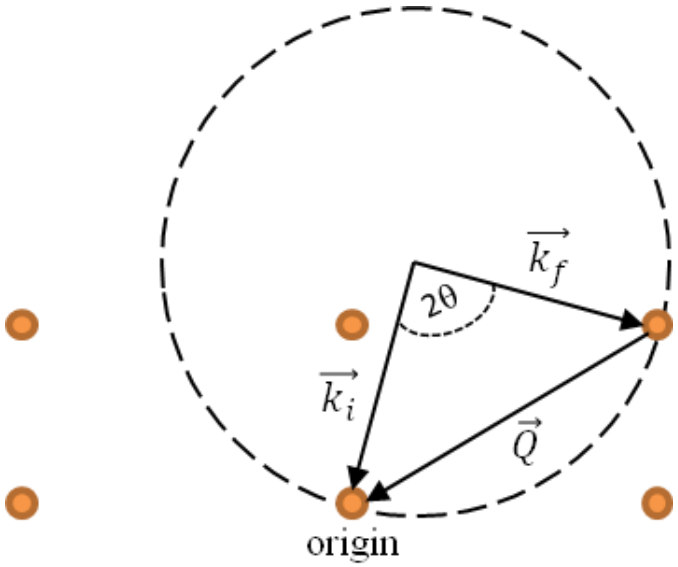

Figure 2.1.Scattering triangle for $\vec{\boldsymbol{Q}} = \vec{\boldsymbol{\tau}}$

The elastic magnetic cross section is given by (Squires 1978)

$$\left(\frac{d\sigma_M}{d\Omega}\right)(\vec{\boldsymbol{Q}}) = \frac{(\gamma r_o)^2}{2} N \frac{(2\pi)^3}{v_o} \exp(-2W) \sum_{\tau_M} \delta(\vec{\boldsymbol{Q}} - \vec{\boldsymbol{\tau}}_{\boldsymbol{M}})$$

$$\times \sum_{\alpha\beta} (\delta_{\alpha\beta} - \widehat{Q_\alpha}\widehat{Q_\beta}) \sum_{rr'} F_r(\vec{\boldsymbol{Q}}) F_{r'}(\vec{\boldsymbol{Q}}) \qquad (2.5)$$

$$\times \boldsymbol{m}_{r,\beta} \boldsymbol{m}_{r',\alpha} \exp\{i\vec{\boldsymbol{Q}} \cdot (\vec{\boldsymbol{r}} - \vec{\boldsymbol{r}}')\}$$

where r_o is the classical radius of the electron, equal to 2.818×10^{-15} m, γ is a constant with value of 1.913 and $F_r(\vec{\boldsymbol{Q}})$ is the magnetic form factor of atom r, arising from the

Fourier transform of the magnetization distribution of the magnetic atoms. The $\boldsymbol{m}_{r,\beta}$ is the β^{th} Cartesian component of the moment belonging to atom *r*. The $\delta(\vec{\boldsymbol{Q}} - \vec{\boldsymbol{\tau}}_{\boldsymbol{M}})$ term has a similar meaning as in the nuclear Bragg scattering, i.e. the magnetic Bragg scattering occurs only for $\vec{\boldsymbol{Q}} = \vec{\boldsymbol{\tau}}_{\boldsymbol{M}}$**.** The vector $\vec{\boldsymbol{\tau}}_{\boldsymbol{M}}$ is the reciprocal lattice vector of the magnetic structure which is usually written as

$$\vec{\boldsymbol{\tau}}_{\boldsymbol{M}} = \vec{\boldsymbol{\tau}} + \vec{\boldsymbol{k}} \tag{2.6}$$

where $\vec{\boldsymbol{k}}$ represents the magnetic periodicity and is known as the wave or propagation vector of the magnetic structure (see Figure 2.2). In order to get a better understanding, we will apply equation (2.5) to the simplest type of magnetic order, which is ferromagnetic.

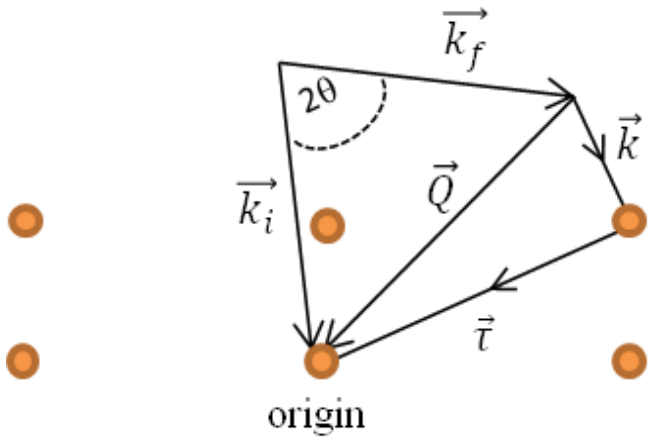

Figure 2.2. Scattering triangle showing the relation between the scattering vector $\vec{\boldsymbol{Q}}$ and the propagation vector $\vec{\boldsymbol{k}}$. Note that in ferromagnetic order, where $\vec{\boldsymbol{k}} = 0$, the Bragg relation $\vec{\boldsymbol{Q}} = \vec{\boldsymbol{\tau}}$ is obtained.

In ferromagnetic order, the magnetic periodicity is identical to the crystallographic periodicity, i.e. the magnetic contributions simply add to the nuclear

contributions in the reciprocal space (in Figure 2.2, $\vec{\boldsymbol{k}} = 0$). Furthermore, in ferromagnetic order the moments are parallel to each other. Assuming that all moments point in only one direction, denoted z, we can simplify equation (2.5) using

$$\begin{aligned}\left|\sum_r \boldsymbol{m}_{r,z} \exp\left(i\vec{\boldsymbol{Q}}\cdot\boldsymbol{r}\right)\right|^2 &= \sum_r \boldsymbol{m}_{r,z} \exp\left(i\vec{\boldsymbol{Q}}\cdot\vec{\boldsymbol{r}}\right) \\ &\times \sum_r \boldsymbol{m}_{r',z} \exp(i\vec{\boldsymbol{Q}}\cdot\vec{\boldsymbol{r}}') \\ &= \sum_{rr'} \boldsymbol{m}_{r,\beta}\boldsymbol{m}_{r',\alpha} \exp\{i\vec{\boldsymbol{Q}}\cdot(\vec{\boldsymbol{r}}-\vec{\boldsymbol{r}}')\}\end{aligned} \tag{2.7}$$

therefore, equation (2.5) can be written as

$$\begin{aligned}\left(\frac{d\sigma_M}{d\Omega}\right)(\vec{\boldsymbol{Q}}) = \frac{(\gamma r_o)^2}{2} N \frac{(2\pi)^3}{v_o} \exp(-2W) \sum_\tau \delta\left(\vec{\boldsymbol{Q}}-\vec{\boldsymbol{\tau}}\right) \\ \times \sum_{\alpha\beta}(\delta_{\alpha\beta} - \widehat{Q_\alpha}\widehat{Q_\beta}) \sum_r (F_r(\vec{\boldsymbol{Q}})\,\boldsymbol{m}_r \exp\{i\vec{\boldsymbol{Q}}\cdot\vec{\boldsymbol{r}}\})^2\end{aligned} \tag{2.8}$$

Based on the above assumption, we can see that the $\sum_{\alpha\beta}(\delta_{\alpha\beta} - \widehat{Q_\alpha}\widehat{Q_\beta})$ term can be simplified, since we only consider one direction of the moment. If we define a unit vector $\hat{\eta}$ for the moment direction of $\boldsymbol{m}_r$ **,** we obtain

$$\sum_{\alpha\beta}(\delta_{\alpha\beta} - \widehat{Q_\alpha}\widehat{Q_\beta})\,\hat{\eta}_\alpha\hat{\eta}_\beta = 1 - \left(\hat{Q}\cdot\hat{\eta}\right)^2 \tag{2.9}$$

then equation (2.8) becomes

$$\begin{aligned}\left(\frac{d\sigma_M}{d\Omega}\right)(\vec{\boldsymbol{Q}}) = \frac{(\gamma r_o)^2}{2} N \frac{(2\pi)^3}{v_o} \exp(-2W) \sum_\tau \delta\left(\vec{\boldsymbol{Q}}-\vec{\boldsymbol{\tau}}\right) \\ \times \left(1 - \left(\hat{Q}\cdot\hat{\eta}\right)^2\right) \sum_r (F_r(\vec{\boldsymbol{Q}})\,\boldsymbol{m}_r \exp\{i\vec{\boldsymbol{Q}}\cdot\vec{\boldsymbol{r}}\})^2\end{aligned} \tag{2.10}$$

For the powder diffraction, in most cases (except structures with high symmetry such as cubic) the $1-\left(\hat{Q}\cdot\hat{\eta}\right)^2$ term enables us to determine the direction of the magnetic moment. If the net magnetic moment $\boldsymbol{m}$ is parallel to the reciprocal lattice vector $\vec{\boldsymbol{\tau}}$ (recall Bragg relation, $\overrightarrow{\boldsymbol{Q}}=\vec{\boldsymbol{\tau}}$), then $1-\left(\hat{Q}\cdot\hat{\eta}\right)^2=0$ and $\left(\frac{d\sigma_M}{d\Omega}\right)\left(\overrightarrow{\boldsymbol{Q}}\right)=0$, i.e. there will be no magnetic scattering contributions. For example, if one observes no magnetic intensity at the (*h 0 0*) peak, that implies that the moments must be parallel to the crystallographic a-axis. However, as mentioned earlier, this simple method cannot be used in the high symmetry structures such as cubic, because one would still see magnetic intensity at the (*h 0 0*) peak position even though the moments are parallel to the a-axis, since in a cubic system (*h 0 0*) is equivalent to (*0 h 0*) and (*0 0 h*), and the $1-\left(\hat{Q}\cdot\hat{\eta}\right)^2$ term is non-zero for the last two reflections.

2.2. Magnetic Space Groups

In crystallography, there are 230 possible space groups, which are made from the combination of all available symmetry operations (point groups, glides and screws) with the Bravais translations. These have been developed to describe crystal structures. These space groups are tabulated in the International Tables for Crystallography (2005). In the case of a magnetic crystal, we have to replace point atoms with axial vector moments, as we must consider both the location and the orientation of the magnetic moments in order to describe fully a magnetic structure. However, since the magnetic moment is an axial vector which may be visualized as an Ampèrian current loop, and not a polar vector that simply indicates a direction, the symmetry operations that were developed to describe the crystal structures are insufficient to describe magnetic structures.

The time-reversal operator (1′ or usually indicated with the primed symmetry operator) is added to the symmetry elements used to describe the crystal structure to construct new groups called magnetic groups (Prandl 1978). The time-reversal operator is equivalent to a time transformation, e.g. $t' = -t$, which changes the rotational direction of a current loop, hence resulting in a further set of symmetry operations. Figure 2.3 illustrates the effect of adding the time-reversal operator. It can be seen that an unprimed mirror symmetry will reverse a current loop whose normal lies parallel to the mirror plane, thus reversing the axial vector, but does not reverse the axial vector that lies perpendicular to the mirror plane. The primed mirror symmetry will reverse the axial vector that lies perpendicular to the anti-mirror plane but not the axial vector that lies parallel to the plane.

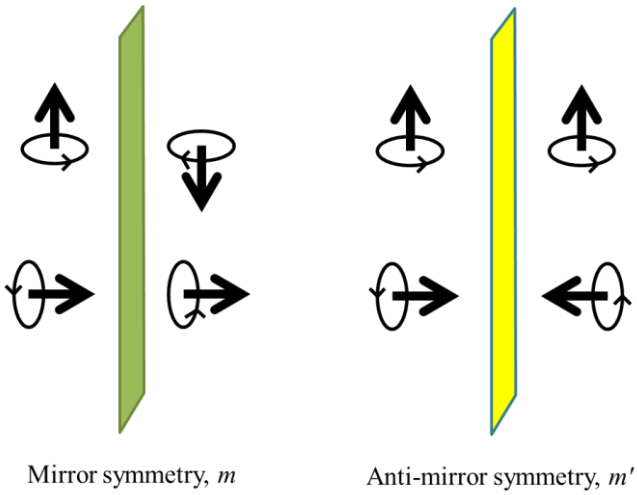

Figure 2.3. The effect on axial vectors of adding the time-reversal operator to a mirror symmetry.

The combination of the primed and unprimed symmetry operators leads to a total of 1651 magnetic space groups known as Shubnikov groups.

2.3. Magnetocrystalline Anisotropy

As mentioned earlier in Chapter 1, the RGa compounds possess a large magnetocrystalline anisotropy (MCA), in which the magnetization process is different when the field is applied along different crystallographic axes. One of the origins of the MCA in the rare-earth compounds is the interaction of the 4f electrons with the electric charges of the surrounding lattices, known as the crystal field interaction. In this section, we will focus on the crystal field interaction as one of the origins of the MCA in the RGa compounds. More detailed treatments of crystal field theory can be found in Hutchings (1964) and Barbara et al. (1988), therefore only a brief discussion of the crystal field interaction will be presented here.

The MCA determines the anisotropy energy (E_a), which may be described by a series expansion in $\sin^2\theta$. Relevant to our work, the anisotropy energy in an orthorhombic cell can be written as (Cadogan et al. 2000)

$$E_a = K_0 + (K_1 + K_1' \cos 2\phi) \sin^2\theta + (K_2 + K_2' \cos 2\phi + K_2' \cos 4\phi) \sin^4\theta + (K_3 + K_3' \cos 2\phi + K_3'' \cos 4\phi + K_3''' \cos 6\phi) \sin^6\theta \quad (2.11)$$

where the polar angles θ and ϕ represent the direction of magnetization relative to the c- and a-axes respectively. The K_0, K_1, K_1' ... K_3''' are the anisotropy constants and are related to the crystal field parameters (see Cadogan et al. (2000) for more detailed derivations). The crystal field interactions of the R ions with the surrounding charges can be described by the crystal field hamiltonian (Hutchings 1964)

$$H_{CF} = \sum_{n=0}^{6} \sum_{m=0}^{n} B_{nm} O_{nm} \quad (2.12)$$

where the O_{nm} are the Stevens operator equivalents, which are polynomials in the angular momentum operators J_z, J_x and J_y (Stevens 1952). The B_{nm} are the crystal field parameters and are given by

$$B_{nm} = A_{nm}\langle r^n \rangle \theta_n \tag{2.13}$$

where $\langle r^n \rangle$ are the 4f radial expectation values and the θ_n are known as the Stevens coefficients, frequently indicated by α_J, β_J and γ_J for n = 2, 4 and 6 respectively. Their values for the R^{3+} ions are listed in Table 2.1. The A_{nm} are the crystal field coefficients. Their values determine the strength of the crystal field parameters B_{nm} and depend on the crystal structure.

For the 4f electrons (l = 3), the summation of n is restricted to n = 6, since they cannot have multipole charge distributions with n > 6. Moreover, the odd terms of n are omitted because for n odd the O_{nm} terms vanish due to the inversion symmetry of the crystal field potential (Buschow & De Boer 2003, Kuz'min & Tishin 2007). The trivial n = 0 term is usually neglected because its effect is only to shift all energy levels by the same amount (Kuz'min & Tishin 2007). Therefore, in practice, the above summation is only over n = 2, 4 and 6.

The simplest method to calculate the coefficients A_{nm} is the point-charge model (Hutchings 1964) in which the coefficients A_{nm} are given by

$$A_{nm} = \frac{4\pi e}{2n+1} \sum_i \frac{Q_i}{R_i^{n+1}} Y_{nm}(\theta_i, \phi_i) \tag{2.14}$$

where $Y_{nm}(\theta_i, \phi_i)$ are the spherical harmonic polynomials. The summation is evaluated over all neighbouring charges Q_i and their corresponding positions (R_i, θ_i, ϕ_i) relative to the origin atom being considered. The problem with this model is that all surrounding

ions are considered as point charges, also the magnitude and the sign of Q_i in most cases is not accurately known. This is particularly problematic in the case of metallic compounds due to conduction electrons. However, since the distances between the origin atom and its neighbouring atoms are known, this model can be used to predict A_{nm}, which can be compared with the experimental values.

In this work, the R^{3+} ions occupy the 4c sites in the orthorhombic *Cmcm* cell with the *m2m* point symmetry. The appropriate crystal field Hamiltonian for the R^{3+} site is given by (Cadogan et al. 2000)

$$H_{CF} = B_{20}O_{20} + B_{22}O_{22} + B_{40}O_{40} + B_{42}O_{42} + B_{44}O_{44} + B_{60}O_{60} + B_{62}O_{62} + B_{64}O_{64} + B_{66}O_{66} \quad (2.15)$$

There are nine crystal field parameters in the above Hamiltonian $\{B_{20}... B_{66}\}$, but in general, the second-order crystal field parameter B_{20} is the most important term in determining the easy magnetization direction of the magnetic materials just below the ordering temperature. In a crystal with uniaxial symmetry, i.e. the c-axis is unique, if $B_{20} < 0$ then the easy magnetization direction is along the c-axis, whereas if $B_{20} > 0$ the easy magnetization direction is perpendicular to the c-axis. (see Buschow & De Boer (2003) for a more detailed discussion).

The signs and magnitudes of the crystal field parameters can be obtained by experimental methods such as inelastic neutron scattering, measurement of the temperature dependence of the specific heat, as well as single-crystal susceptibility measurements. The latter method has been employed to determine the second order crystal field parameters (B_{20} and B_{22}) in the RGa compounds (listed in Table 1.3) by Shohata (1977) and Shohata et al. (1974). Following Aleonard et al. (1969), Shohata et

al. deduced the second-order crystal field parameters using the following equations,

$$\theta_a = \theta + \frac{(2J-1)(2J+3)(B_{20}+B_{22})}{10k_B}$$

$$\theta_b = \theta - \frac{(2J-1)(2J+3)B_{20}}{5k_B} \tag{2.16}$$

$$\theta_c = \theta + \frac{(2J-1)(2J+3)(B_{20}-B_{22})}{10k_B}$$

where θ_a,θ_b, and θ_c are the paramagnetic Curie temperatures along the a, b and c-axes, respectively. The θ is the paramagnetic Curie temperature due to the molecular field, which can be expressed as

$$\theta = \frac{\lambda g^2 {\mu_B}^2 J(J+1)}{3k_B} \tag{2.17}$$

where g and λ are the Landé g-factor and the Weiss molecular field constant, respectively. Given that the values of θ_a, θ_b, and θ_c are known from experiment, one can then determine exactly the signs and magnitudes of the second-order crystal field parameters (B_{20} and B_{22}).

Table 2.1. The total angular momenta (J) and the Stevens coefficients for the R^{3+} ions (Stevens 1952).

$\mathbf{R^{3+}}$	$\boldsymbol{J}$	$\boldsymbol{\alpha_J \times 10^{-2}}$	$\boldsymbol{\beta_J \times 10^{-4}}$	$\boldsymbol{\gamma_J \times 10^{-6}}$
Ce^{3+}	5/2	-5.7143	63.4921	0.0000
Pr^{3+}	4	-2.1010	-7.3462	60.9940
Nd^{3+}	9/2	-0.6428	-2.9111	-37.9880
Sm^{3+}	5/2	4.1270	25.0120	0.0000
Eu^{3+}	0	0.0000	0.0000	0.0000
Gd^{3+}	7/2	0.0000	0.0000	0.0000
Tb^{3+}	6	-1.0101	1.2244	-1.1212
Dy^{3+}	15/2	-0.6349	-0.5920	1.0350
Ho^{3+}	8	-0.2222	-0.3330	-1.2937
Er^{3+}	15/2	0.2540	0.4440	2.0699
Tm^{3+}	6	1.0101	1.6325	-5.6061
Yb^{3+}	7/2	3.1746	-17.3160	148.0001

2.4. Mössbauer effect

2.4.1. Introduction

The Mössbauer effect is the recoil free emission of a γ-ray photon by a nucleus and its subsequent recoilless absorption by an identical nucleus. It was discovered by Rudolph Mössbauer (1958) for which he was awarded the Nobel Prize in 1961. The Mössbauer effect has been detected in at least 88 γ-ray transitions in 72 isotopes of 42 different elements and has been an important technique in physics, chemistry and biology (Greenwood & Gibb 1971)

In this work, ^{155}Gd and ^{166}Er Mössbauer spectroscopy will be used to study hyperfine interactions in GdGa and ErGa. Figures 2.4 and 2.5 show the decay schemes associated with ^{166}Er and ^{155}Gd Mössbauer spectroscopy. The ^{155}Gd Mössbauer spectroscopy uses the 86.5 keV level which is populated by the β^- decay of ^{155}Eu, whereas ^{166}Er Mössbauer spectroscopy uses the 80.65 keV level which is populated by the β^- decay of ^{166}Ho.

2.4.2. Hyperfine Interactions

A nucleus may interact with electric and magnetic fields from its surrounding environments. Such interactions are known as hyperfine interactions and can shift energy levels and lift their degeneracy. In the Mössbauer effect, there are three types of hyperfine interaction, namely the electric monopole interaction, the magnetic dipole interaction and the electric quadrupole interaction. In the following sections, these interactions will be discussed briefly. More detailed discussions can be found in Gonser (1975) and Greenwood & Gibb (1971)

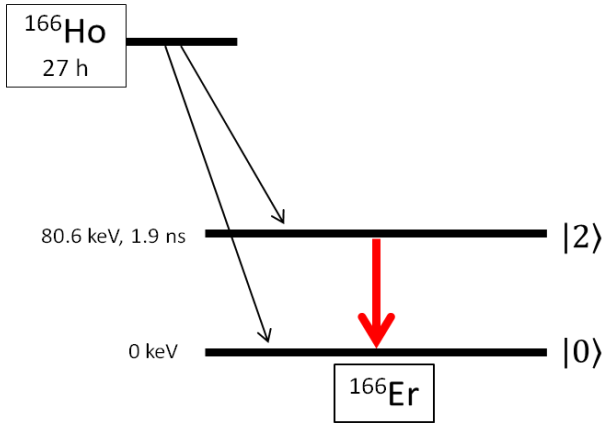

Figure 2.4. Decay scheme associated with ^{166}Er Mössbauer spectroscopy

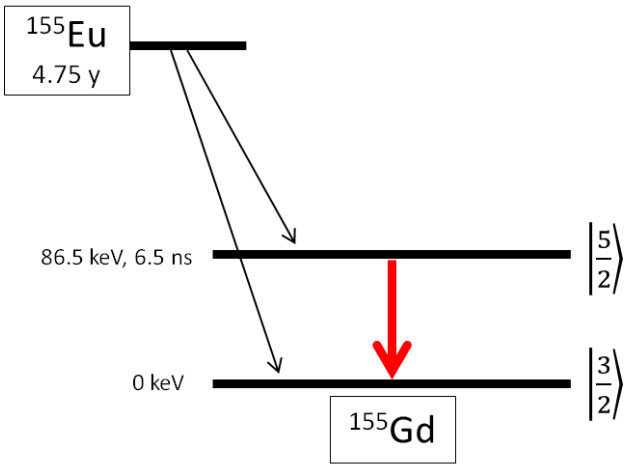

Figure 2.5. Decay scheme associated with ^{155}Gd Mössbauer spectroscopy

2.4.3. Electric Monopole Interaction

This interaction arises due to the finite size of the nucleus and the electric charge density from the s-electrons within it, resulting in a Coulombic interaction between them. This interaction has the effect of shifting all energy levels by varying amounts and is

known as the isomer shift (δ). Following Greenwood & Gibb (1971), the isomer shift is given by

$$\delta = \frac{2\pi}{5} Z|e|^2(\langle {R_e}^2 \rangle - \langle {R_g}^2 \rangle)(|\psi(0)|_a^{\ 2} - |\psi(0)|_s^{\ 2}) \tag{2.18}$$

where $\langle {R_e}^2 \rangle$ and $\langle {R_g}^2 \rangle$ are the mean square radii of the excited and ground nuclear states. $|\psi(0)|_a^{\ 2}$ and $|\psi(0)|_s^{\ 2}$ are the s-electron densities at the absorber and source nuclei, respectively. This shift is normally reported with respect to a standard, such as the source or a reference absorber.

2.4.4. Magnetic Dipole Interaction

A nucleus with a non zero spin $\vec{I}$ has a magnetic moment $\vec{\mu}$, which interacts with internal hyperfine fields acting at the nucleus (e.g. Cadogan & Ryan (2006)). The interaction is described by the following Hamiltonian

$$\begin{aligned} H_M &= -\vec{\mu} \cdot \vec{B}_{hf} \\ &= -g_n \mu_N \hat{I} \cdot \vec{B}_{hf} \end{aligned} \tag{2.19}$$

where μ_N is the nuclear magneton, $\vec{B}_{hf}$ is the hyperfine magnetic field and g_n is the g-factor of the nuclear state in question. The corresponding eigenvalues of the above magnetic Hamiltonian are

$$E_M = -m_I g_n \mu_N B_{hf} \tag{2.20}$$

where $m_I = I, I-1 \ldots -I$ is the nuclear azimuthal spin quantum number. It can be seen that this interaction splits a nuclear state $|I\rangle$ into $2I+1$ equally spaced states.

Related to this work, the ^{166}Er nucleus has excited and ground states of $|I=2\rangle$ and $|I=0\rangle$ respectively. In the presence of the magnetic dipole interaction, the excited

state will split into five levels, while the ground state does not split. The allowed transitions obey the selection rules for the dipole transition with $\Delta I = 2$, $\Delta m = 0, \pm 1, \pm 2$, giving five possible Mössbauer transitions. Moreover, in ^{166}Er Mössbauer spectra, the relative intensities are 1:1:1:1:1.

The ^{155}Gd nucleus has excited and ground states of $\left|I = \frac{5}{2}\right\rangle$ and $\left|I = \frac{3}{2}\right\rangle$ respectively. Under the influence of the magnetic dipole interaction, the excited state splits into six levels, and the ground state splits into four levels. The allowed transitions are $\Delta m_{\mathrm{I}} = 0, \pm 1$, giving twelve possible Mössbauer transitions with the relative intensities of 10:6:3:1:4:6:6:4:1:3:6:10 (Figure 2.6).

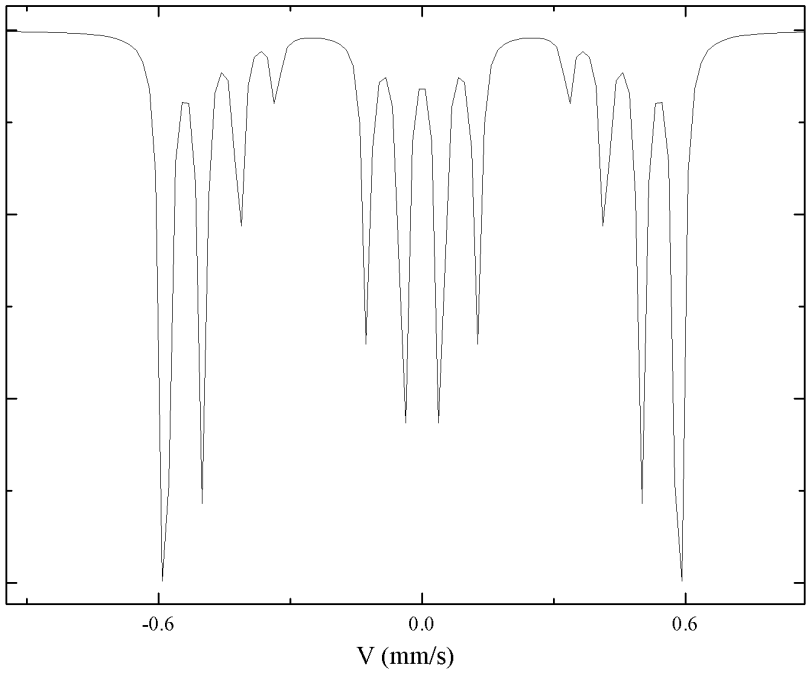

Figure 2.6. Simulated spectrum of ^{155}Gd with B_{hf} = 20 T, $eQVzz$ = 0, η = 0 and line width of Γ = 0.05 mm/s. A small Γ was chosen to make the transitions more clearly resolved. (Drawn using the MOSPLV software (Chipaux 1990)).

2.4.5. Electric Quadrupole Interaction

A nucleus with spin $I > \frac{1}{2}$ has a non-spherical charge distribution and thus possesses a non-zero quadrupole moment (Q) which represents the deviation of the nuclear charge from spherical symmetry. Such nuclei can interact with an inhomogeneous electric field described by the electric field gradient (EFG) at the nucleus. The EFG is a 3×3 second rank tensor that has contributions from the unfilled electron shells, valence electrons, and surrounding lattice charges and may be written in the form (Gonser 1975)

$$V_{ij} = \frac{\partial^2 V}{\partial i \, \partial j} \quad (i, j = x, y, z) \tag{2.21}$$

where V_{ij} are the EFG tensor components and V is the electrostatic potential at the nucleus. The diagonal elements of V_{ij} are dependent, since they must satisfy the Laplace equation

$$V_{xx} + V_{yy} + V_{zz} = 0 \tag{2.22}$$

in other words, the EFG tensor is traceless. A unique axis system known as the principal axis frame of the EFG is defined such that the off-diagonal terms disappear and

$$|V_{zz}| \geq |V_{yy}| \geq |V_{xx}| \tag{2.23}$$

Furthermore, it is convenient to introduce the asymmetry parameter

$$\eta = \frac{V_{xx} - V_{yy}}{V_{zz}} \tag{2.24}$$

which represents the deviation of the EFG from uniaxial symmetry. Based on equation (2.23), the value of η is restricted to $0 \leq \eta \leq 1$. With this standard terminology, the electric quadrupole Hamiltonian may be written in the form

$$H_Q = \frac{eQV_{zz}}{4I(2I-1)}\left[3\hat{I}_z{}^2 - \hat{I}^2 + \frac{\eta(\hat{I}_+{}^2 + \hat{I}_-{}^2)}{2}\right] \tag{2.25}$$

I is the nuclear spin quantum number, $\hat{I}$ is the nuclear spin operator, $\hat{I}_\pm = \hat{I}_x \pm i\hat{I}_y$ are raising and lowering operators, and $\hat{I}_x, \hat{I}_y, \hat{I}_z$ are the nuclear spin component operators (Greenwood & Gibb 1971).

For the 4f electrons, there are two sources which contribute to the total EFG, namely the 4f electron shell and the surrounding lattice charges. Thus, the diagonal EFG tensor components can also be expressed as (Stewart 1985, Stewart et al. 2000)

$$V_{zz} = -k_{4f}\langle O_{20}\rangle_T - k_{latt}A_{20} \tag{2.26}$$

$$V_{xx} - V_{yy} = -3k_{4f}\langle O_{22}\rangle_T - k_{latt}A_{22} \tag{2.27}$$

where

$$k_{4f} = -\frac{\theta_2|e|}{4\pi\epsilon_0}(1-R_Q)\langle r^{-3}\rangle_{4f}$$
$$k_{latt} = \frac{4}{e}\frac{(1-\gamma_\infty)}{(1-\sigma_2)} \tag{2.28}$$

The θ_2 is the second-order Stevens coefficient appropriate for the rare earth in question and R_Q is the atomic Sternheimer effect. The $(1-R_Q)$ term represents the correction to the 4f quadrupole interaction due to the screening of the valence electrons from the nucleus by inner shell electrons (Gonser 1975). The γ_∞ and σ_2 are the Sternheimer antishielding factor and the lattice shielding factor respectively. The $(1-\gamma_\infty)$ term represents the enhancement of the lattice quadrupole interaction, due to the distortion of the closed electron shell by the surrounding lattice charges. Moreover, the first terms in (2.26) and (2.27) correspond to the temperature-dependent contribution due to the crystal field distortion of the 4f shell, and the second terms are the contribution from the

surrounding lattice charges which is relatively independent of temperature (lattice contraction or expansion gives some temperature dependence to this term). $\langle O_{20} \rangle_T$ and $\langle O_{22} \rangle_T$ are the Boltzmann averages of the Stevens operators over the thermally populated crystal field levels. A_{20} and A_{22} are the second-order crystal field coefficients.

2.4.6. Mixed Magnetic and Quadrupole Interactions

The Hamiltonian for mixed magnetic and quadrupole interactions is given by (e.g. Cadogan & Ryan (2004))

$$\begin{aligned} H_{total} &= H_Q + H_M \\ &= \frac{eQV_{zz}}{4I(2I-1)}\left[3\hat{I}_z{}^2 - \hat{I}^2 + \frac{\eta\left(\hat{I}_+{}^2 + \hat{I}_-{}^2\right)}{2}\right] + g_n\mu_N\hat{I}\cdot\vec{B}_{hf} \\ &= \frac{eQV_{zz}}{4I(2I-1)}\left[3\hat{I}_z{}^2 - \hat{I}^2 + \frac{\eta\left(\hat{I}_+{}^2 + \hat{I}_-{}^2\right)}{2}\right] + \\ &\quad g_n\mu_N B_{hf}(I_z\cos\theta + [I_x\cos\phi + I_y\sin\phi]\sin\theta) \end{aligned} \tag{2.29}$$

where θ and ϕ are the polar angles of the R^{3+} magnetic moment relative to the principal axes of the EFG. In general, the total Hamiltonian can be quite complex since the principal axes of the EFG and the reference axes of the magnetic moment may not coincide. The energy level splittings relevant to ^{166}Er in the presence of the magnetic and quadrupole interactions are shown in Figure 2.7.

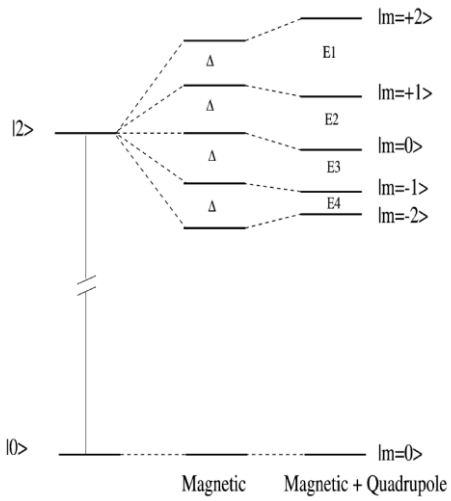

Figure 2.7. Energy level splitting in ^{166}Er (Cadogan & Ryan 2004)

2.5. The Rietveld Method

2.5.1. Introduction

The Rietveld method was developed by Hugo Rietveld (Rietveld 1969) and has been successfully applied to determining the structure of materials from x-ray and neutron powder diffraction data. This method had an advantage over the other powder methods at that time, since it was able to refine a diffraction pattern that contained many overlapping reflections. This section will focus on the general formulation of the Rietveld method including a discussion about the criteria of fit in this method. Readers should refer to Young (1993) and McCusker et al. (1999) for more detailed discussions.

2.5.2. General Formulation

Basically, the Rietveld method uses a non-linear least squares algorithm to minimize the residual function S_y which is given by

$$S_y = \sum_i w_i \left(y_i^{exp} - y_i^{calc}\right)^2; \qquad w_i = \frac{1}{y_i^{exp}} \tag{2.30}$$

where y_i^{exp} and y_i^{calc} are the observed and calculated intensites at the i[th] data point. The summation is evaluated over all data points. In general, for a given powder diffraction pattern there are many Bragg reflections contributing to the y_i^{exp}. The intensities of these reflections (I_K) are proportional to the square of the absolute value of the structure factor $|F_K|^2$ where *K* stands for the Miller indices *h, k, l*. Based on that information, the calculated intensities can be determined from the calculated values of $|F_K|^2$ derived from a given structural model, including also the contribution from the instrumental geometry and the background. Thus, the calculated intensities can be written in the form

$$y_i^{calc} = s \sum_K L_K \, |F_K|^2 \phi(2\theta_i - 2\theta_K) P_K A + y_{bi} \tag{2.31}$$

where *s* is the scale factor and L_K contains the Lorentz-polarization and multiplicity factor. The Lorentz-polarization factor depends on the instrumental geometry, detector, monochromator, and sample positioning, whereas the multiplicity factor can be defined as the number of different crystal planes which have the same spacings. ϕ is the reflection profile function, P_K is the preferred orientation function, *A* is an absorption factor and y_{bi} is the background intensity at the i[th] data point. In the following discussions, some of these terms will be discussed briefly.

The structure factor F_K takes the form

$$F_K = \sum_j N_j f_j e^{-\frac{8\pi^2 u^2 \sin^2\theta}{\lambda}} e^{2\pi i(hx_j + ky_j + lz_j)} \tag{2.32}$$

where *h, k, l* are the Miller indices, x_j, y_j, z_j are the coordinates of the j[th] atom in the unit

cell, N_j is the site occupancy multiplier for the j[th] atom which is equal to the actual site occupancy divided by the general site multiplicity. f_j is the atomic scattering factor and u^2 is the root mean square thermal displacement of the j[th] atom. This term will determine the intensity of the calculated scattering peak.

In equation (2.31), the reflection profile function $\phi(2\theta_i - 2\theta_K)$ approximates the effects of both instrumental and specimen features of the reflection profile, such as transparency and broadening. There are many profile functions that have been developed, e.g Gaussian, Lorentzian, Pseudo-Voigt, Pearson VII, etc. The profile term also contains parameters which determine the width of the peak intensity (FWHM) and is typically modelled as (Cagliotti et al. 1958)

$$FHWM^2 = U\tan^2\theta + V\tan\theta + W \tag{2.33}$$

where U, V and W are refineable parameters.

The absorption factor A varies with instrument geometry. For neutron powder diffraction experiments where the sample holder is usually a cylindrical Vanadium can, the absorption correction factor is given by (Dwiggins 1975)

$$A = \frac{1}{\pi R^2}\int_0^R \int_0^{2\pi} \exp\Big(-\mu\{[R^2 - r^2\sin^2(\theta+\varphi)]^{\frac{1}{2}} + [R^2 - r^2\sin^2(\theta-\varphi)]^{\frac{1}{2}}\} \times \cosh(2\mu R\sin\theta\cos\varphi\Big) r dr d\varphi \tag{2.34}$$

where R is the radius of the cylinder, μ is the linear absorption of the sample and θ is the Bragg angle. A numerical table related to the above equation is given in Table 6.3.3.2 in the International Tables for Crystallography vol. C (Maslen 2004).

Related to our work, this correction was employed to the raw neutron diffraction

data of DyGa (section 4.2) via

$$y_i^{corr} = \frac{y_i^{exp}}{A_i} \tag{2.35}$$

The Lobanov/Alte da Veiga absorption function (Lobanov & Alte da Veiga 1998) was then employed in the refinement of the corrected patterns. This empirical function for $A_b\lambda = \mu R < 3$ cm^{-1} is given by

$$A_h = \exp[-k_0\, A_b\lambda - k_1(A_b\lambda)^2 - k_2(A_b\lambda)^3 - k_3(A_b\lambda)^4] \tag{2.36}$$

where

$$\begin{aligned} k_0 &= 1.697653 \\ k_1 &= \left(25.99978 - 0.01911 \sin^{\frac{1}{2}}\theta\right)\exp(-0.024514 \sin^2\theta) \\ &\quad + 0.109561 \sin\theta - 26.0456) \\ k_2 &= -0.02489 - 0.39499 \sin^2\theta + 1.219077 \sin^3\theta \\ &\quad - 1.31268 \sin^4\theta + 0.871081 \sin^5\theta - 0.2327 \sin^6\theta \\ k_3 &= 0.003045 + 0.018167 \sin^2\theta - 0.03305 \sin^4\theta \end{aligned} \tag{2.37}$$

2.5.3. Criteria of Fit

The quality of the fit to the observed data can be given numerically and is usually done in terms of agreement indices or *R* values (McCusker et al. 1999). Several fitting criteria that are now commonly used are given below

$$R_F = \frac{\sum_K \left|{F_K}^{exp} - {F_K}^{calc}\right|}{\sum_K |{F_K}^{exp}|} \tag{2.38}$$

$$R_{Bragg} = \frac{\sum_K \left|{I_K}^{exp} - {I_K}^{calc}\right|}{\sum_K |{I_K}^{exp}|} \tag{2.39}$$

$$R_{exp} = \left[\frac{(N-P)}{\sum_i^N w_i (y_i{}^{exp})^2}\right]^{1/2} \tag{2.40}$$

$$R_{wp} = \left[\frac{\sum_i w_i \, (y_i{}^{exp} - y_i{}^{calc})^2}{\sum_i \; w_i (y_i{}^{exp})^2}\right]^{1/2} \tag{2.41}$$

and the "goodness of fit" indicator is given by

$$GOF = \frac{R_{wp}}{R_{exp}} \tag{2.42}$$

2.6. Summary

In this chapter, we have discussed the theoretical background relevant to our work, encompassing a discussion of magnetic neutron scattering, Mössbauer effect, crystal field interactions and the Rietveld method.

3. Experimental Methods

3.1. Sample Preparation

All polycrystalline samples of RGa (R = Gd, Dy, Ho and Er) were prepared by arc melting the consituent elements of purity better than 99.9 wt% under a high purity argon atmosphere (less than 1 ppm impurity). The elements used in the sample preparation were purchased from Alfa Aesar. It was found necessary to add an excess of 2-3% of rare earth before melting, in order to compensate for weight loss during melting. To ensure that no unaccounted for weight loss had occurred, the samples were weighed before and after melting.

A schematic diagram of the argon arc furnace is shown in Figure 3.1. The argon arc furnace has a tungsten electrode and a copper hearth. An electric discharge between the positive tungsten electrode and the negative copper hearth in the chamber filled with argon gas will create an argon arc (plasma). This arc or plasma can be used to melt any type of metal. Both electrode and copper hearth are water-cooled.

The melting process can be described in the following way. First, pieces of R and solid gallium were transferred to the water cooled copper hearth with the R pieces placed on top of the gallium. This procedure was done to ensure that both elements are mixed well during the melting because gallium has a very low melting temperature (~30^0 C) and it will splash around if the electric arc directly hits it. The pressure inside the chamber was then pumped down to lower than 5 kPa, and flushed again with high purity argon gas. To ensure that there was no oxygen inside the chamber, this pumping and flushing process was repeated at least 4 times. The chamber was then filled with high purity argon

gas, and the initial electric current was set to ~70A. The constituent elements were then melted together. After the first melting, the resulting ingot was turned over and re-melted with a higher current of ~80 A. This process was repeated at least twice to ensure the homogeneity of the sample. The resulting ingots were crushed and powdered using a mortar and pestle. No samples required post-annealing since it was found that annealing did not improve the quality of the samples.

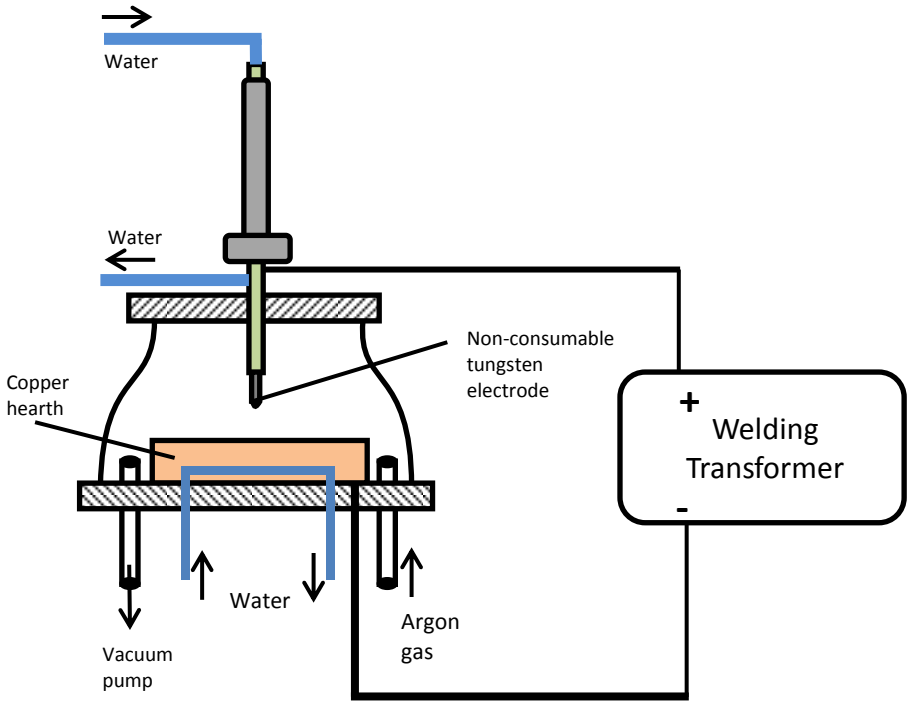

Figure 3.1. Schematic diagram of the argon arc-furnace

3.2. Phase Identification

X-ray powder diffraction was used to identify the phases present in the sample. The measurements were carried out at room temperature using Cu-Kα radiation on the PANalytical X'Pert Pro and SIEMENS D500 diffractometers. The data were collected in the 2θ range $15\text{-}80^0$ with a step width of $2\theta = 0.02^0$. All x-ray diffraction patterns were analyzed by the Rietveld method using the Fullprof/WinPlotr suite (Rodríguez-Carvajal 1993, Roisnel & Rodríguez-Carvajal 2001).

3.3. Bulk Resistivity Measurement

Electrical resistivity measurements on HoGa were made using a four-point probe method. The data were taken at 1 K intervals from 5 to 180 K in a JANIS SHI-950-X closed-cycle helium refrigerator. The sample was cut from the large ingots into a small rectangular shape of approximately 10 mm length and 3 mm × 3 mm in cross section. The voltage and current contacts made with 20 μm diameter gold wire were bonded on the polished surface of the sample using silver paste. The voltage across the sample was recorded using a lock-in amplifier model SR530 from Stanford Research System, while a constant alternating current of 0.23 mA / 55 Hz was passed through the sample.

3.4. Neutron Powder Diffraction

Neutron diffraction measurements on the DyGa and HoGa samples were made on the *Echidna* high resolution powder diffractometer at the OPAL reactor in Sydney, Australia (Liss et al. 2006). The data were collected at various temperatures in the range of 3 K – 125 K with a neutron wavelength of 1.6220(5) Å. The effects of the high neutron

absorption associated with the rather high (50 at.%) Dy content of the DyGa sample were included in the Rietveld refinement of the neutron diffraction data using the Lobanov/Alte da Veiga absorption function (Lobanov & Alte da Veiga 1998) as implemented in the GSAS/EXPGUI package (Toby 2001, von Dreele & Larson 2004). The HoGa patterns were corrected for absorption effects and refined via the Rietveld method using the Fullprof/Winplotr suite (Rodríguez-Carvajal 1993, Roisnel & Rodríguez-Carvajal 2001).

Figure 3.2. C2 High Resolution Powder Diffractometer (NRC-CNBC 2009)

Neutron diffraction measurements on GdGa were carried out on the C2 multi-wire high resolution powder diffractometer (DUALSPEC) at the NRU reactor, Canadian Neutron Beam Centre, Chalk River, Ontario (Figure 3.2). The data were collected at three different temperatures of 220 K, 110 K and 3.6 K. Natural gadolinium is the strongest neutron absorbing element, therefore the high Gd content of the GdGa sample (50 at.%) will entirely absorb the incoming neutron beam from the reactor, making it impossible to obtain a diffraction pattern using the standard Vanadium can as a sample holder. A flat-

plate sample mounting technique (Ryan & Cranswick 2008) was employed to obtain a usable diffraction pattern. Basically, this technique uses a flat-plate sample holder with silicon single-crystal windows in which the powder sample is thinly spread and covers a significant area of the incoming neutron beam, thus simply turning the powder into a 'thin film' (Figure 3.3). It is worth mentioning that the neutron absorption of natural Gd also varies rapidly with the neutron energy (Lynn & Seeger 1990). The absorption cross-section has a value of 49700 b (almost 20 times larger than Cd, a commonly used neutron shielding material) for $\lambda = 1.80$ Å (Lynn & Seeger 1990) and decreases to ~35000 b at $\lambda = 1.33(1)$ Å (Cadogan et al. 2009). Thus, in order to minimize the neutron absorption cross-section we used the shorter neutron wavelength of 1.33(1) Å. No absorption correction was applied and analyses of the patterns were accomplished via the Rietveld method using the Fullprof/Winplotr suite (Rodríguez-Carvajal 1993, Roisnel & Rodríguez-Carvajal 2001). All magnetic structures derived from the neutron diffraction refinements were drawn using the Fullprof Studio Program (Chapon & Rodríguez-Carvajal 2008).

Figure 3.3. Photograph of the silicon flat plate sample holder that was used to obtain the neutron diffraction patterns of GdGa (Ryan & Cranswick 2008).

3.5. ^{155}Gd and ^{166}Er Mössbauer Spectroscopy

^{166}Er Mössbauer spectroscopy on ErGa and ^{155}Gd Mössbauer spectroscopy on GdGa were carried out in the Centre for the Physics of Materials at the Physics Department, McGill University, Montreal, Quebec (Ryan 2011). The ^{155}Gd Mössbauer pattern was obtained at 5 K in transmission mode using a neutron-irradiated $^{154}SmPd_3$ source prepared at the NRU reactor, Canadian Neutron Beam Centre, Chalk River, Ontario. The spectrometer's drive system was calibrated using a laser interferometer and velocities were cross-checked against ^{57}CoRh/α-Fe at room temperature and the ^{155}Gd Mössbauer spectrum of $GdFe_2$ at 5 K. The temperatures of both sample and source were maintained at 5 K. The spectrum was fitted using a non-linear least squares algorithm to the full nuclear hyperfine Hamiltonian for the ^{155}Gd 5/2 → 3/2 transition.

The ^{166}Er Mössbauer spectra were obtained at various temperatures in the range of 5 – 35 K using ^{166}Ho sources prepared by neutron-activation of $Ho_{0.6}Y_{0.4}H$ in the SLOWPOKE reactor at Ecole Polytechnique, Montreal. The spectrometer was calibrated using the 819.4 T magnetic splitting in $ErFe_2$ at 1.4 K. All spectra were fitted using a non-linear least squares algorithm to the full nuclear hyperfine Hamiltonian. A dynamic model as proposed by Blume & Tjon (1968) was included in the fitting process to account for the electronic relaxation effects in the ^{166}Er Mössbauer spectra.

3.6. Summary

In this section, we have described briefly the experimental techniques that were used in this work, including sample preparation and other techniques relevant to our study of the magnetic structures and spin reorientations in RGa compounds.

4. Magnetic structures of DyGa and HoGa

4.1. Phase identification

Both HoGa and DyGa compounds were prepared in an argon arc furnace. The detail of the arc melting procedures have been discussed in section 3.1. The arc-melted ingots were crushed and checked with x-ray powder diffraction. Figure 4.1 shows the refinement of the x-ray diffraction patterns for both samples. The refinements confirmed the formation of the CrB-type *Cmcm* orthorhombic structure. Both R (Ho and Dy) and Ga atoms occupy 4c sites, generated by the special atomic position (0 y ¼). The refined values of the positional y parameters are 0.3590(3) for the Dy and 0.0766(6) for the Ga in DyGa. For HoGa, the refined values of the positional y parameters are 0.3600(4) for the Ho and 0.0782(5) for the Ga. Any impurity phases present amounted to less than 1 wt%, indetectable in the powder diffraction pattern. The refined lattice parameters along with the conventional R-factor fit indicators for HoGa and DyGa are summarized in Table 4.1.

Table 4.1. The refined lattice parameters at room temperature and conventional R-factor values of DyGa and HoGa

	Lattice parameters (Å)			**Refinement indicators**		
	a	**b**	**c**	**R_F**	**R-Bragg**	**GOF**
DyGa	4.2929(7)	10.866(6)	4.0627(7)	15.4	13.5	1.4
HoGa	4.2774(4)	10.787(8)	4.0446(4)	8.95	14.5	1.3

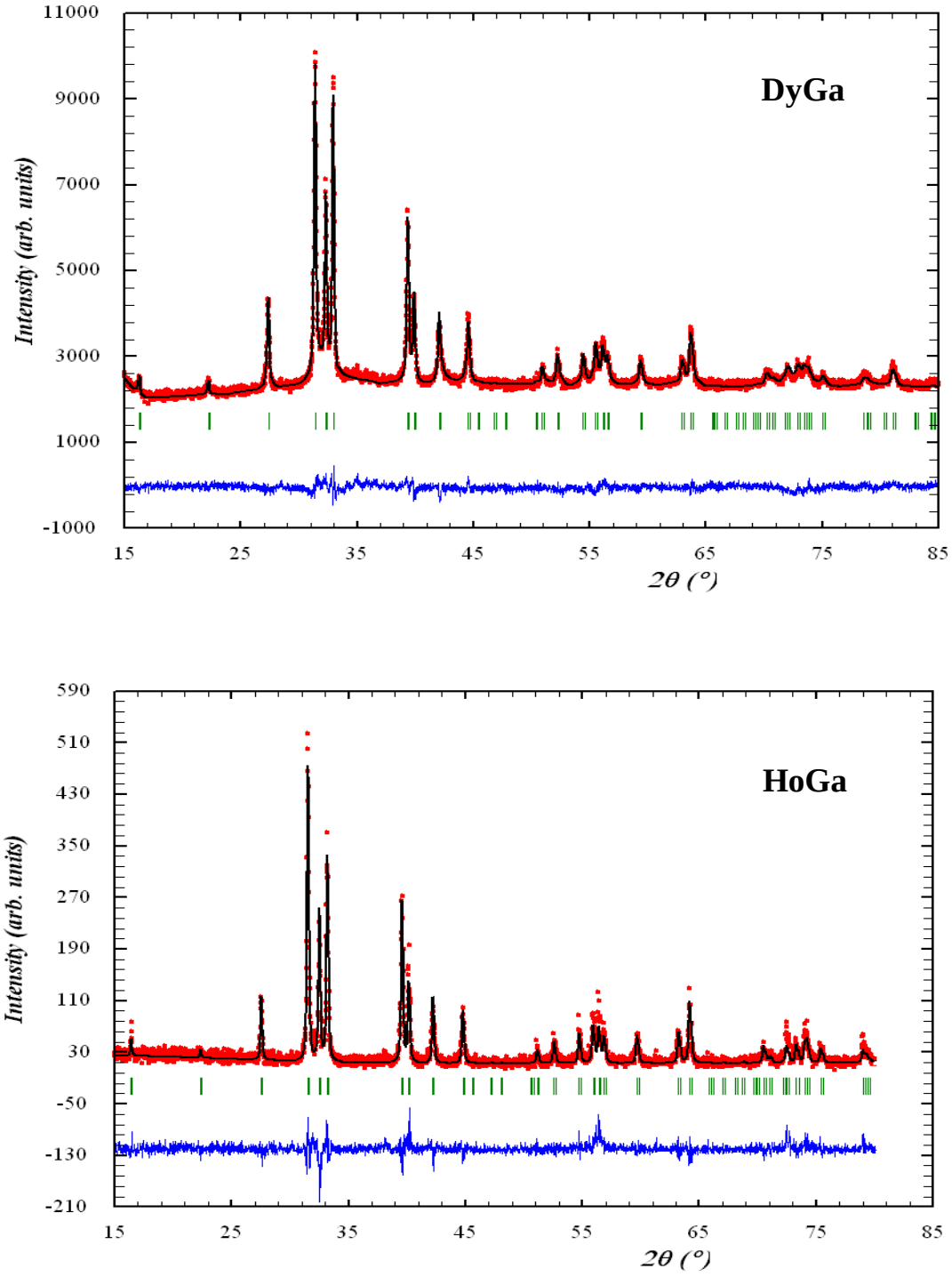

Figure 4.1.X-ray powder diffraction patterns of DyGa and HoGa obtained at 295 K with Cu–Kα radiation. Red dots, black, and blue lines indicate the observed, calculated and difference patterns respectively. The vertical red lines indicate the Bragg markers

4.2. Magnetic structure of DyGa

Neutron powder diffraction patterns of DyGa were recorded at 125 K and 3 K. DyGa is a ferromagnet with a Curie temperature of 115(2) K (Fujii et al. 1971, Iraldi et al. 1974, Shohata et al. 1974, Shohata 1977, Nesterov et al. 1992, Delyagin et al. 2007), therefore the 125 K pattern corresponds to the nuclear scattering and was used to determine the crystal structure, whereas the 3 K pattern comprises both nuclear and magnetic scattering and was used to determine the magnetic structure of this compound.

The neutron diffraction patterns of DyGa at 125 K and 3 K are shown in figure 4.2. The refined lattice parameters at 125 K are a = 4.2980(3) Å, b = 10.8537(6) Å, c = 4.0592(3) Å. The refinement shows no unfitted peaks. The conventional R-factors for this refinement are R_p = 2.78, R_{wp} = 2.21 and χ^2 = 1.86.

The diffraction pattern recorded at 3 K shows considerable magnetic contributions from the Dy sublattice. There are no additional peaks that would indicate antiferromagnetic order and all magnetic contributions simply add to the existing Bragg nuclear peaks, thus the propagation vector **k** is [0 0 0]. In order to determine the magnetic ordering mode for DyGa, we carried out symmetry analysis for the Dy site. There are sixteen possible magnetic space groups corresponding to the *Cmcm* spacegroup associated with Dy atoms at the 4c sites. Eight of these magnetic space groups involve anti-C order (C_p) and can be ruled out since they necessarily produce antiferromagnetic structures, due to the fact that moments related by the C translation $+\left[\frac{1}{2}\ \frac{1}{2}\ 0\right]$ are antiparallel. The remaining eight magnetic space groups are shown in Table 4.2. The only magnetic space groups that produce ferromagnetic order of the Dy sublattice in DyGa are *Cmc'm'*, *Cm'cm'* and *Cm'c'm* with ferromagnetic order along the orthorhombic

crystal a, b and c-axes respectively.

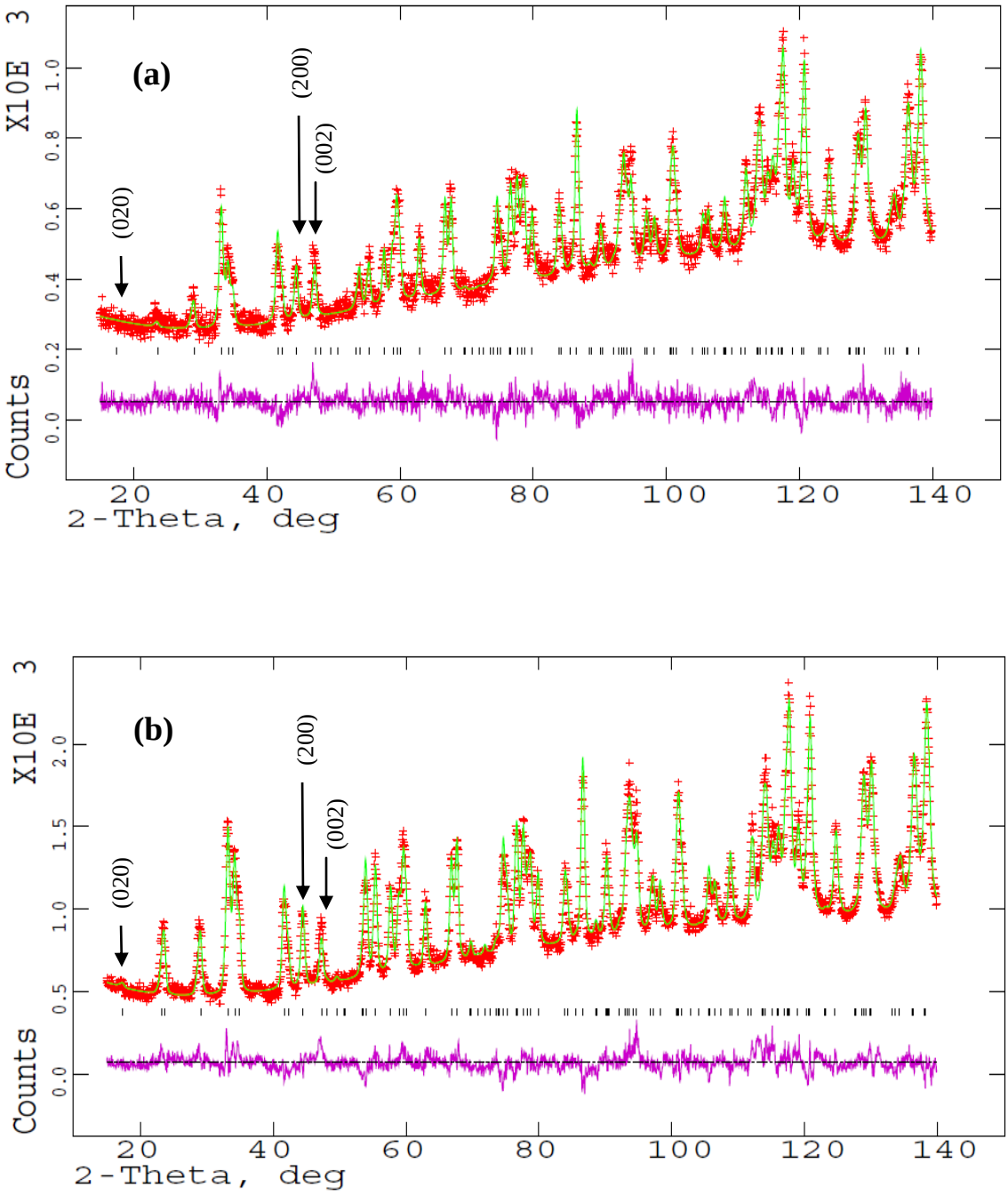

Figure 4.2. Neutron powder diffraction patterns of DyGa obtained at (a) 125 K and (b) 3 K, with a neutron wavelength of 1.6220(5) Å. Arrows indicate three important peaks used in determining the direction of the Dy magnetic moments (see text).

Table 4.2. Magnetic space groups belonging to *Cmcm* on the 4c site associated with a *C* magnetic lattice. X, Y, Z indicate non-zero components of the magnetic moment (Prandl 1978)

	Atomic positions			
	0, y, 1/4	**0, −y, 3/4**	**½, y+½, 1/4**	**½, −y+½, 3/4**
Cmcm				
Cm'cm	+Z	−Z	+Z	−Z
Cmc'm				
Cmcm'	+X	−X	+X	−X
Cm'c'm	Z	Z	Z	Z
Cmc'm'	X	X	X	X
Cm'cm'	Y	Y	Y	Y
Cm'c'm'	+Y	−Y	+Y	−Y

The direction of the Dy magnetic moments can be determined as follows. From Figure 4.2, one can see considerable magnetic contributions to the (020) and (200) peaks. On the other hand, there is no magnetic intensity at the (002) position. These observations clearly indicate ferromagnetic order of the Dy sublattice along the c-axis corresponding to the *Cm'c'm* magnetic space group. The refinement of the 3 K pattern using the *Cm'c'm* magnetic space group is satisfactory with the conventional R-factors of R_p = 4.87, R_{wp} = 3.78 and χ^2 = 2.26.. We also find a refined Dy magnetic moment of 9.6(3) μ_B, which is essentially the 'free-ion' value for the Dy^{3+} ion (gJ = 10).

The observation of a full Dy moment at 3 K is in complete agreement with the result of the ^{161}Dy Mössbauer spectroscopy study of DyGa by Iraldi et al. (1974). The observation of c-axis magnetic order is also consistent with the signs and relative magnitudes of the diagonal and off-diagonal second-order crystal field terms derived from single-crystal susceptibility measurements by Shohata (1977) which are listed in Table 1.3.

4.3. Bulk resistivity measurement on HoGa

Figure 4.3 shows the temperature dependence of the normalized electrical resistivity of HoGa. It can be seen that this compound shows metallic behaviour at high temperature, i.e. the resistivity increases linearly with increasing temperature. The data show a clear change in slope at around 63 K. A weak change in slope is also observed in the resistivity around 19 K.

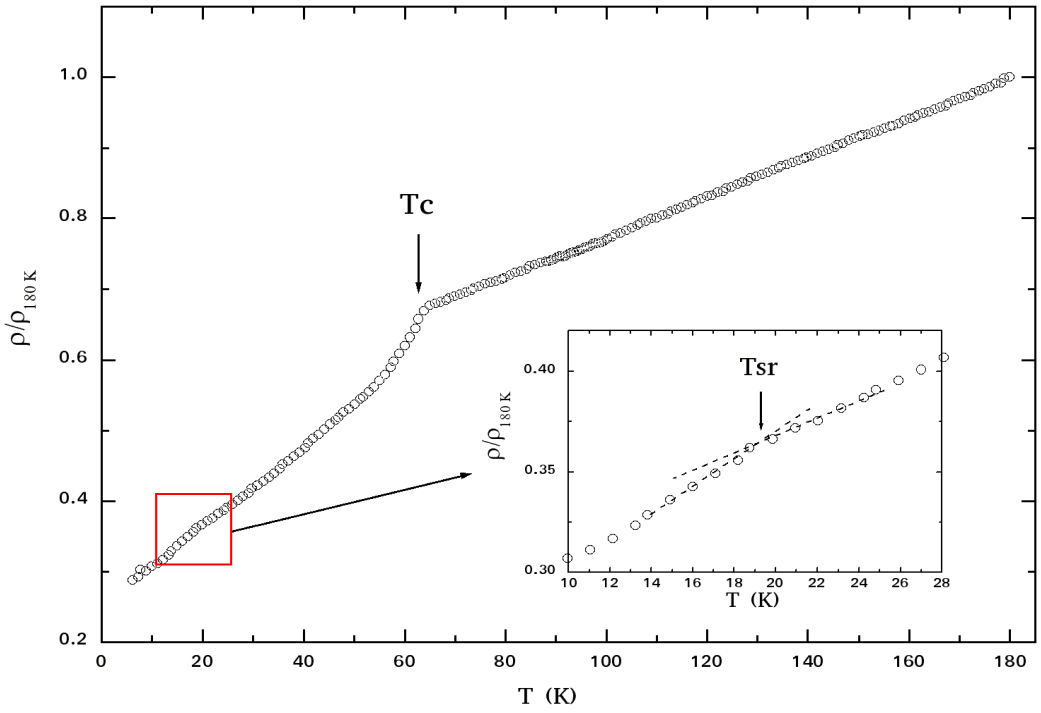

Figure 4.3. Normalized resistivity of HoGa. Arrows indicate the first and second transitions

The observation of these two transitions is in complete agreement with the previous results from magnetic measurements and ^{119}Sn Mössbauer spectroscopy on HoGa (Delyagin et al. 2007, Chen et al. 2010), thus confirming that the first (at 63 K) and second transition (at 19 K) in our resistivity measurement are related to the transition

from the paramagnetic state to the ferromagnetic state and the spin reorientation transition, respectively.

4.4. Magnetic structure and spin reorientation of HoGa

4.4.1. Neutron Powder Diffraction

Neutron powder diffraction patterns of HoGa were recorded at 80 K, 45 K, 22 K and 4 K. HoGa is a ferromagnet with a Curie temperature of 66(3) K (Shohata 1977, Nesterov et al. 1992, Delyagin et al. 2007, Chen et al. 2010), therefore the 80 K pattern corresponds to the nuclear scattering from the orthorhombic *Cmcm* cell and was used to determine the lattice and atomic positions parameters. The refinement shows no unfitted peaks. Table 4.3 shows the refined atomic positions for HoGa at 80 K. The conventional R-factors for this refinement are R_p = 15.9, R_{wp} = 13.7 and χ^2 = 2.33.

Table 4.3. The atomic positions for HoGa, refined from the neutron diffraction pattern at 80 K

Atom	x	y	z
Ho	0	0.3592(3)	¼
Ga	0	0.0750(6)	¼

The diffraction patterns recorded at 45 K, 22 K and 4 K show considerable magnetic contributions from the Ho sublattice. There are no extra peaks that would indicate antiferromagnetic order and all magnetic contributions simply add to the existing Bragg nuclear peaks, i.e. the propagation vector **k** is [0 0 0]. We used a similar refinement approach as in the case of DyGa. As before, we can immediately rule out the antiferromagnetic C_p groups. The remaining eight magnetic groups are given in Table

4.2. From these eight possible magnetic space groups, we can rule out the antiferromagnetic space groups *Cm'cm*, *Cmcm'*, and *Cm'c'm'* based on single-crystal susceptibility measurements that clearly indicate ferromagnetic order (Shohata 1977). Thus we are left with three magnetic space groups that produce ferromagnetic order along one of the orthorhombic crystal axes. The observation of substantial magnetic contributions to the (020) and (200) peaks, combined with the absence of any magnetic intensity at the (002) peak, clearly indicates ferromagnetic order along the c-axis, corresponding to the *Cm'c'm* magnetic space group (Figure 4.4). At 45 K, we find a refined Ho magnetic moment of 6.2(2) μ_B. The conventional R-factors for this refinement are R_p = 11.7, R_{wp} = 11.3, R_{mag} = 6.31 and χ^2 = 3.47.

The neutron diffraction pattern collected at 22 K is shown in Figure 4.5. Since similar intensity changes as with the pattern at 45 K were observed, the magnetic structure of the Ho sublattice was determined using the same arguments as those at 45 K. We find a refined Ho magnetic moment of 8.2(2) μ_B pointing along the c-axis at 22 K. The conventional R-factors for this refinement are R_p = 10.0, R_{wp} = 10.4, R_{mag} = 4.51 and χ^2 = 4.55.

Upon further cooling below 22 K, we observe an increase in the magnetic intensity at the (021) peak, relative to the magnetic intensity at the (110) peak (Figure 4.5). Similar changes also occur at other peaks, indicating that the Ho magnetic moments cant away from the c-axis. The refinement of the 3 K pattern shows that the canting Ho moments tip towards an intermediate planar arrangement between the crystallographic a- and b-axes. We find canting angles of $\theta = 30(2)^0$ and $\varphi = 49(4)^0$. We also find that the Ho magnetic moments reach 8.8(2) μ_B i.e. the 'free-ion' value (9 μ_B) at 3 K. Figure 4.6

illustrates the difference between the magnetic structure of HoGa at 22 K and 3 K. The conventional R-factors for this refinement are R_p = 7.74, R_{wp} = 8.45, R_{mag} = 2.70 and χ^2 = 3.46. The refined lattice parameters and the refined values of the magnetic moments and orientation of the Ho sublattice at different temperatures are summarized in Tables 4.4 and 4.5 respectively.

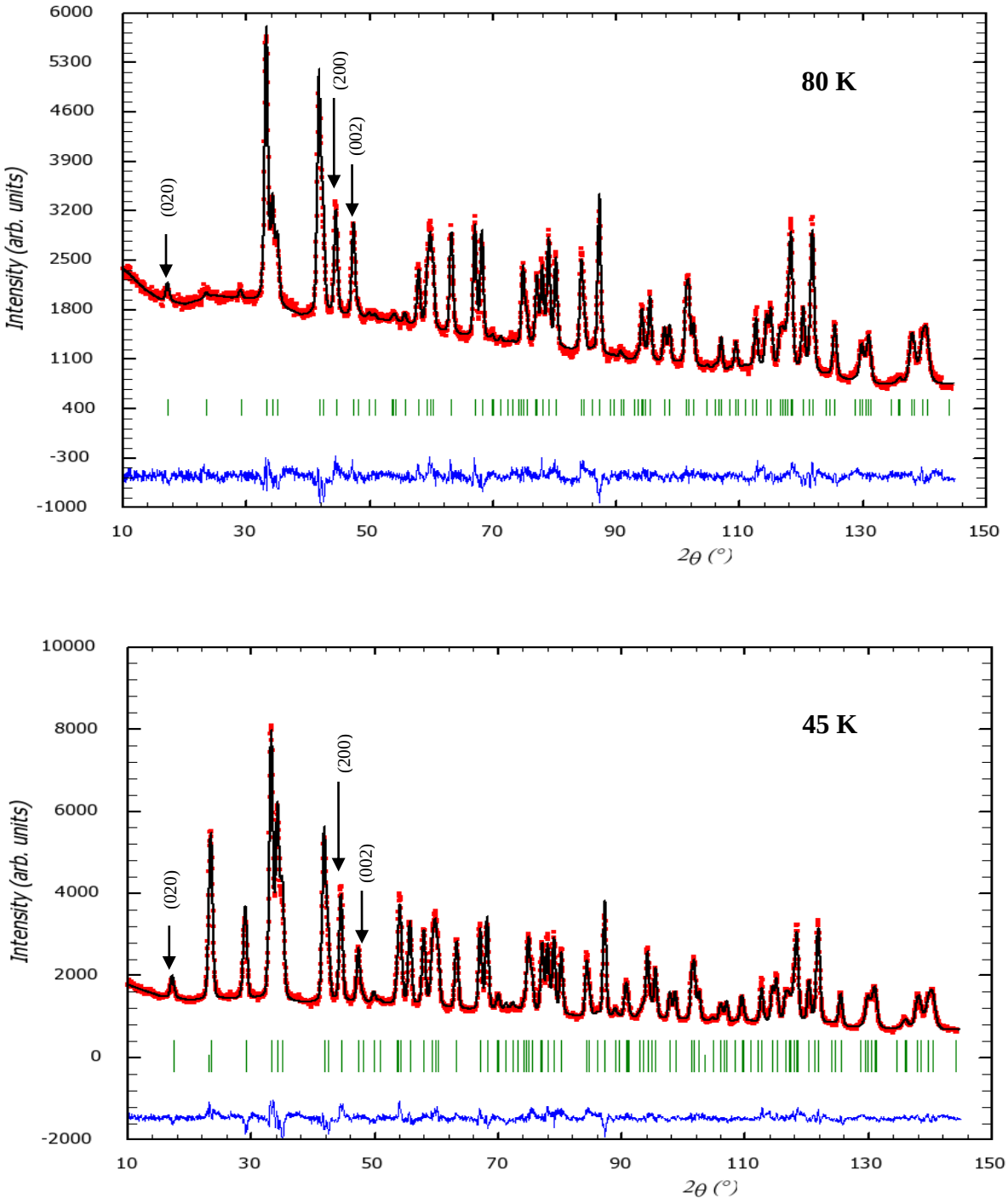

Figure 4.4. Neutron powder diffraction patterns of HoGa collected at 80 K and 45 K with a neutron wavelength of 1.6220(5) Å. Arrows indicate three important peaks used in determining the direction of the Ho magnetic moments

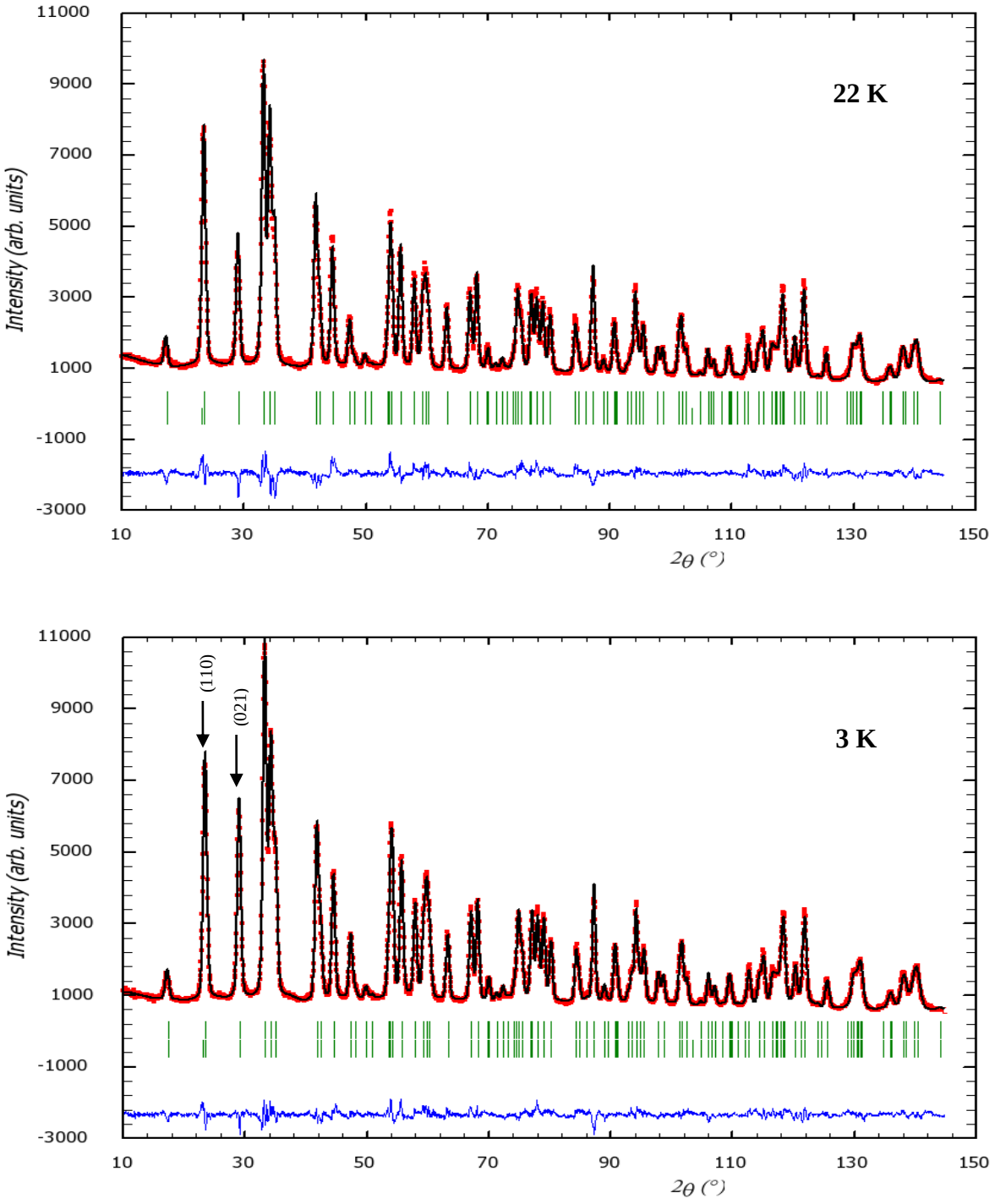

Figure 4.5. Neutron powder diffraction patterns of HoGa collected at 22 K and 3 K with a neutron wavelength of 1.6220(5) Å.

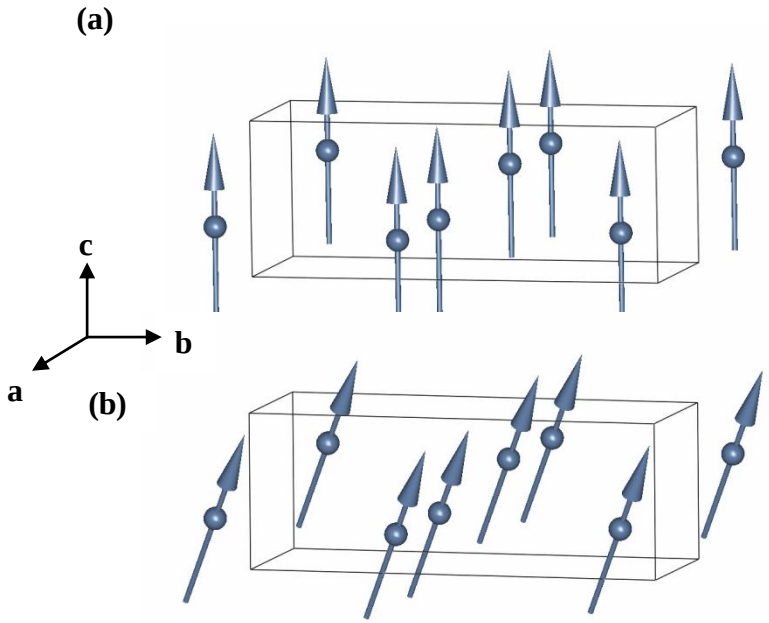

Figure 4.6. Magnetic structure of the Ho sublattice in HoGa at (a) 22 K and (b) 3 K.

Table 4.4.The lattice parameters for HoGa at different temperatures.

T (K)	Lattice parameters (Å)		
	a	b	c
80	4.2779(3)	10.7596(8)	4.0353(3)
45	4.2764(5)	10.7575(10)	4.0345(4)
22	4.2758(5)	10.7582(11)	4.0337(5)
3	4.2763(3)	10.7584(8)	4.0332(3)

Table 4.5.The refined magnetic data for HoGa at different temperatures.

T(K)	Ho moment (μ_B)	θ (^{0})	φ (^{0})
80	0	–	–
45	6.2(2)	0	0
22	8.1(2)	0	0
3	8.8(2)	30(2)	49(4)

The observation of the canted ferromagnetic structure of HoGa which initially orders along the c-axis is in contrast with the ferromagnetic order of the isostructural compound DyGa which shows no spin reorientation upon cooling below T_c (Section 4.2). This difference illustrates the effect of the crystal field acting on the R^{3+} ions in RGa. As shown in Table 4.6, although both ions have negative second- and fourth-order Stevens coefficients, their sixth-order terms have opposite signs. Clearly, the spin reorientation of HoGa is driven by competition between the different crystal field orders, with the higher order (6^{th}) term becoming significant as the temperature is lowered.

The observation of c-axis magnetic order is consistent with the signs and relative magnitudes of the diagonal and off-diagonal second-order crystal field terms derived from single-crystal susceptibility measurements by Shohata (1977) specifically, $B_{20} > 0$ and $B_{22}^c < 0$, where the crystallographic b-axis was taken as the principal axis (Z) of the crystal field Hamiltonian (see Table 1.3).

Table 4.6. Signs of the Stevens coefficients (second-order α_J , fourth-order β_J and sixth-order γ_J) for the Dy^{3+} and Ho^{3+} ions (Elliott & Stevens 1953).

Ions	α_J	β_J	γ_J
Dy^{3+}	−	−	+
Ho^{3+}	−	−	−

4.4.2. The Interpretation of the ^{119}Sn Mössbauer Spectroscopy data on Sn-doped HoGa

As discussed earlier in Chapter 1, Delyagin et al. (2007) used ^{119}Sn doping in the RGa compounds to study the magnetic order of the R sublattice by ^{119}Sn Mössbauer Spectroscopy. They showed that the EFG axes are collinear with the orthorhombic axes, as expected from the *m2m* point symmetry of the Ga 4c sites, with the particular identification of the EFG axes being (ZXY) = (abc). Within this EFG frame, the temperature dependence of the quadrupole splitting showed that above about 20 K the hyperfine field makes an angle of 90^0 with the Z(EFG) axis, along the Y(EFG) axis. In other words, Ho magnetic ordering is along the c-axis, consistent with the result from our neutron diffraction. At 5 K, Delyagin et al. deduced a canting angle of 58^0, with the hyperfine field lying in the YZ(EFG) plane, i.e. Ho magnetic order in the crystallographic ac-plane. In Figure 4.7 we show the orientational relationship between the Mössbauer and neutron diffraction results, in terms of the crystal (abc) and EFG (XYZ) axes.

The quadrupole splitting in a magnetically split Mössbauer spectrum can be expressed as

$$QSH = \frac{eQVzz}{8} \times [3\cos^2\alpha - 1 + \eta(\sin^2\alpha)\cos(2\beta)] \qquad (4.1)$$

where α and β are the polar angles of the hyperfine field in the principal axis frame of the EFG and η is the asymmetry parameter of the EFG tensor. Delyagin et al. (2007) deduced *eQVzz* = 1.10(8) mm/s and η = 0.65(9). Hence, using the canting angle of α = 58^0 and β = 90^0, they obtain the observed value of *QSH* = − 0.087(4) mm/s.

As mentioned before, we find canting angles of θ = 30(2)^0 and φ = 49(4)^0 relative to the crystallographic c-axis. The principal Z-axis of the EFG frame itself lies along the crystallographic a-axis. It is straightforward to show that our aforementioned angles correspond to α = 71(3)^0 and β = 66(3)^0 in the EFG frame employed in the Mössbauer work. Thus, by using equation (5.1), we get a QSH value of -0.15(4) mm/s, which is consistent with the Mössbauer result.

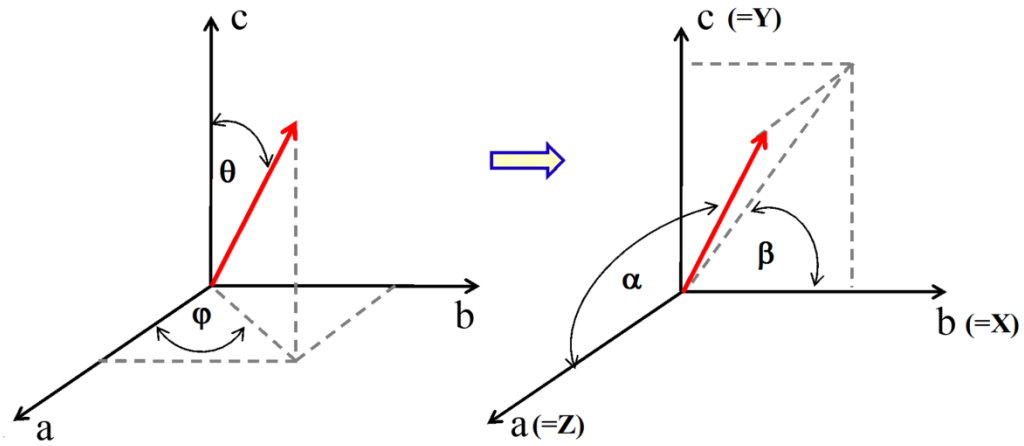

Figure 4.7. Orientation of the Ho magnetic moment relative to the crystal (abc) and EFG (XYZ) axes, used in the interpretation of the neutron powder diffraction and Mössbauer data.

4.5. Summary

We have shown that the magnetic order of the Dy and Ho sublattices in DyGa and HoGa is ferromagnetic along the orthorhombic c-axis below their Curie temperatures. At 3 K, the refined magnetic moments of the Dy and Ho atoms are 9.6(3) μ_B and 8.8(2) μ_B, respectively. We have also shown that below 22 K the Ho moment cant away from the c-axis towards the ab-plane, and at 3 K the Ho magnetic order is defined by the polar angles of $\theta = 30(2)^0$ and $\varphi = 49(4)^0$ relative to the crystallographic c-axis.

5. Magnetic Structure and Spin Reorientation of GdGa

5.1. Phase Identification

Figure 5.1 shows the x-ray powder diffraction pattern of GdGa. Refinement of this pattern confirmed the formation of the CrB-type *Cmcm* orthorhombic structure with impurities of $GdGa_2$ (space group *P6/mmm*) and Gd_2O_3 (space group $Ia\bar{3}$) present in the total amount of less than 4 wt%. The lattice parameters of GdGa are a = 4.3447(6) Å, b = 11.019(11) Å and c = 4.1080(6) Å. The crystallographic data for the Gd and Ga sites are given in Table 5.1.

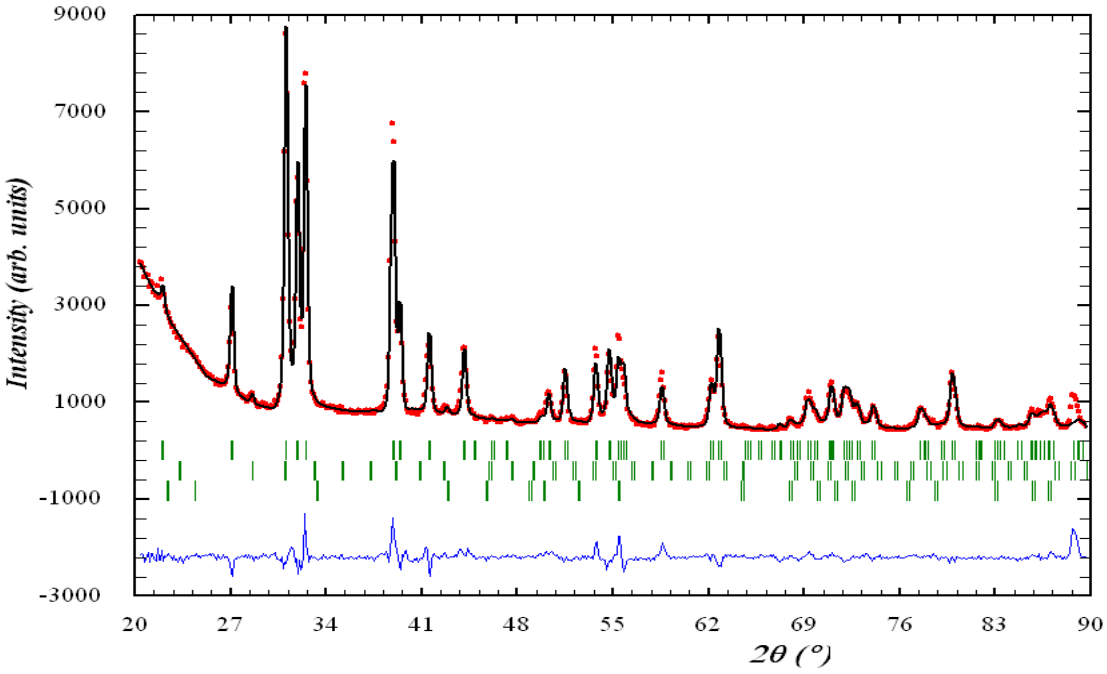

Figure 5.1. X-ray powder diffraction pattern of GdGa collected at room temperature with Cu-Kα radiation. The Bragg markers, from top to bottom, represent GdGa, Gd_2O_3 and $GdGa_2$ respectively.

Table 5.1. Crystallographic data for GdGa.

Atom	x	y	z
Gd	0	0.3614(3)	¼
Ga	0	0.0785(4)	¼

5.2. Neutron Scattering Length of Gd

As shown earlier in Chapter 2, the nuclear cross-section depends on the scattering length of the atom. The scattering length itself is a complex number and varies with the energy of the neutron. In this work, we used the scattering length tabulation by Lynn and Seeger (1990), to determine the scattering length for natural Gd corresponding to our neutron wavelength (λ = 1.33(1) Å and E = 46.34 meV). The values of the real and imaginary parts of the scattering length of natural Gd corresponding to our neutron wavelength are 10.54 fm and -12.66 fm respectively.

5.3. Neutron Powder Diffraction

We have mentioned in section 3.4 that the neutron wavelength was 1.33(1) Å, in order to minimize the absorption cross-section of natural Gd. However, the use of such a neutron wavelength has a disadvantage, since it will compress the diffraction pattern including the magnetic peaks, into a lower scattering angle (2θ), although in this work we are able to distinguish each magnetic peak clearly. Due to the impact of angle-dependent absorption effects (Ryan & Cranswick 2008), and considering the small values of the magnetic form factor of Gd^{3+} at high angles (large Q values), only the data within $5^0 < 2\theta < 36^0$ (0.41 $Å^{-1} < Q < 2.92$ $Å^{-1}$) were considered in the refinement.

Neutron powder diffraction patterns of GdGa were obtained at 220 K, 110 K and

3.6 K. GdGa is a ferromagnet with a Curie temperature of 185(4) K (Shohata 1977, Leithe-Jasper & Hiebl 1996, Delyagin et al. 2007, Zhang et al. 2009), therefore the 220 K pattern corresponds to the nuclear scattering from the orthorhombic *Cmcm* cell and was used to determine the crystal structure. One broad peak at $2\theta \sim 34^0$ was identified as an artefact by comparing data obtained at different times at the same temperature (see Appendix A). Therefore, this artefact was excluded from the refinement. In Figure 5.2, we show the neutron diffraction pattern obtained at 220 K. The refined lattice parameters are a = 4.329(2) Å, b = 11.064(4) Å, c = 4.087(2) Å. Table 5.2 gives the refined atomic positions for GdGa at 220 K.

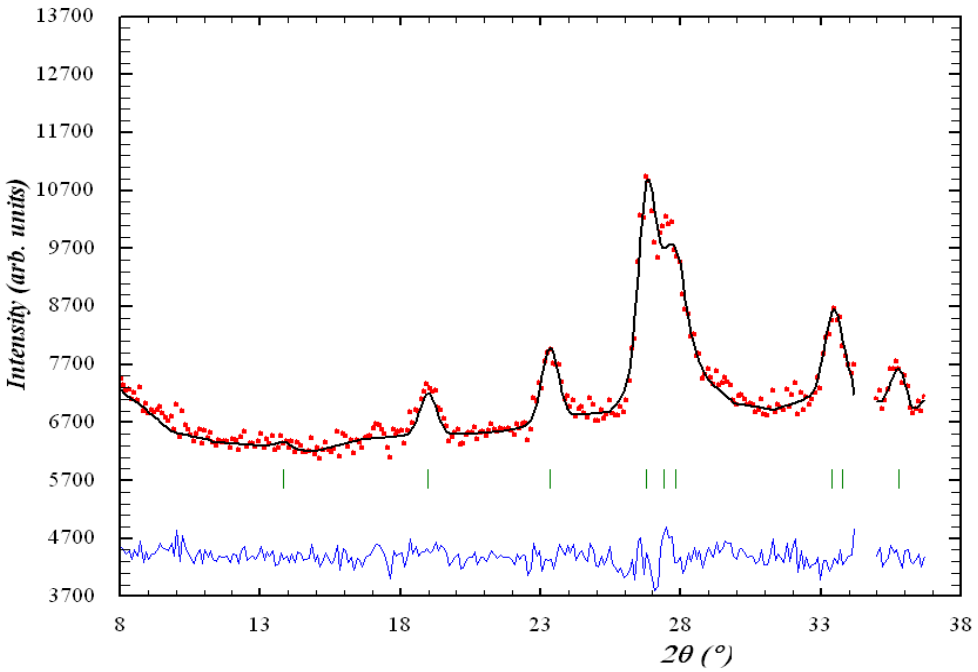

Figure 5.2. Neutron powder diffraction pattern of GdGa collected at 220 K with a neutron wavelength of 1.33(1) Å.

For the low temperature refinements, we used the difference between the high and low temperature patterns (110 K – 220 K and 3.6 K – 220 K patterns) to minimize the ambiguity in the refinements. These difference patterns will reflect only the magnetic contributions of the Gd magnetic moments. The purely nuclear scattering at 220 K was used to set scale factors and the instrument parameters. These parameters were then fixed during the refinement of the difference patterns.

Table 5.2. The atomic positions for GdGa, refined from the neutron diffraction pattern at 220 K

Atom	**x**	**y**	**z**
Gd	0	0.3558(3)	¼
Ga	0	0.1076(7)	¼

Figure 5.3 shows the fitted difference between the 220 K and 110 K patterns. Despite the poor signal-to-noise ratio of the pattern, one is still able to see clear magnetic contributions arising from the magnetic ordering of the Gd sublattice. The strongest magnetic peaks occur at the (110), (021) and (111) positions with scattering angles 2θ = 19.1^0, 23.4^0 and 26.9^0, respectively. All of the magnetic peaks occur at the same scattering angles as the nuclear peaks and no additional peaks were observed, indicating ferromagnetic order of the Gd sublattice with a propagation vector **k** = [0 0 0], therefore a similar approach as used to determine the direction of the Dy and Ho sublattices in DyGa and HoGa (chapter 4) can be employed.

As in the cases of DyGa and HoGa, we can immediately rule out the antiferromagnetic C_p groups. From the eight possible magnetic space groups shown in Table 4.2, we can rule out the antiferromagnetic space groups *Cm'cm*, *Cmcm'*, and

Cm'c'm' based on susceptibility measurements that indicate ferromagnetic order (Leithe-Jasper & Hiebl 1996). The absence of a magnetic contribution to the (020) peak allows us to rule out all magnetic space groups except the *Cm'cm'* space group corresponding to ferromagnetic order along the crystallographic b-axis. At 110 K, we find a refined Gd magnetic moment of 4.6(2) μ_B.

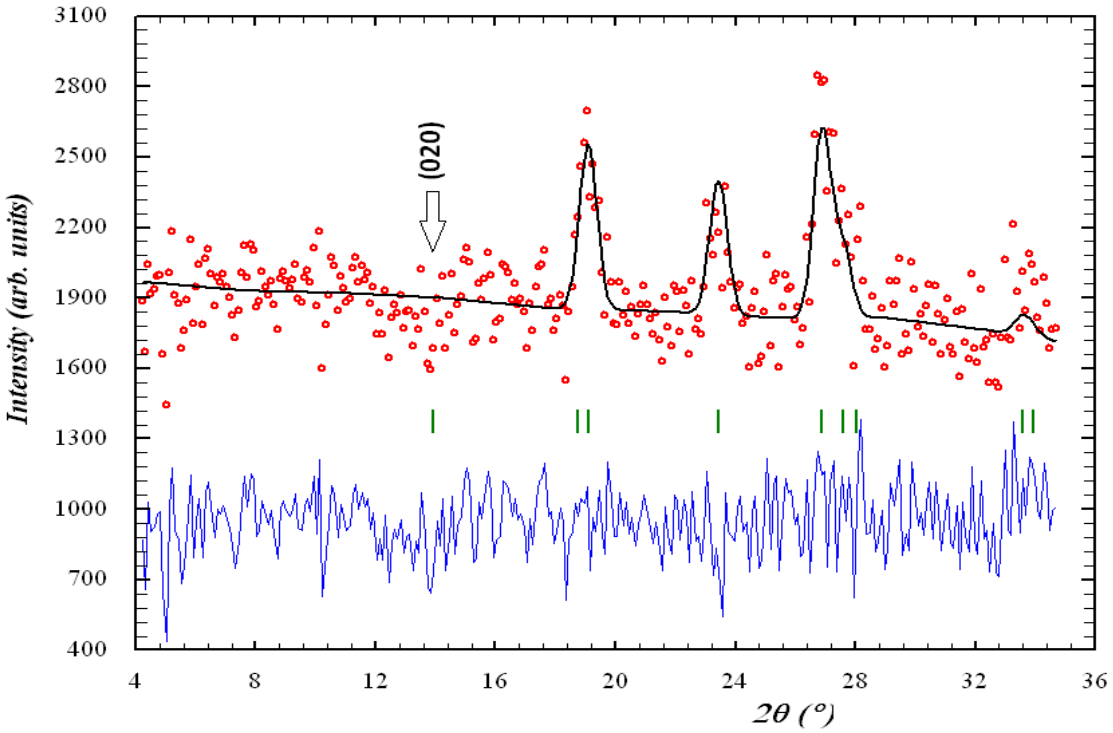

Figure 5.3. The refinement of the difference between the 220 K and 110 K patterns of GdGa using the *Cm'cm'* space group.

Magnetic measurements on GdGa carried out by Zhang et al. (2009) were used to check our refinement. The average magnetization at 110 K can be determined by extrapolation of the isothermal magnetization to zero field. According to their measurement (Figure 3(a) from (Zhang et al. 2009)), the magnetization value of GdGa is about 110 J/T.kg at 110 K, which corresponds to an average moment of 4.47 μ_B/Gd. Our

neutron diffraction refinement at 110 K yields a refined Gd magnetic moment of 4.6(2) μ_B which is in excellent agreement with their result.

The 3.6 K – 220 K difference pattern is shown in Figure 5.4. All of the magnetic peaks occur at the same positions as the nuclear peaks and no additional peaks were observed, indicating ferromagnetic order of the Gd sublattice with a propagation vector **k** = [0 0 0]. We also observe an increase in the magnetic intensity at the (040)/(130) and (110) peaks indicating that the Gd magnetic moments cant away from the b-axis.

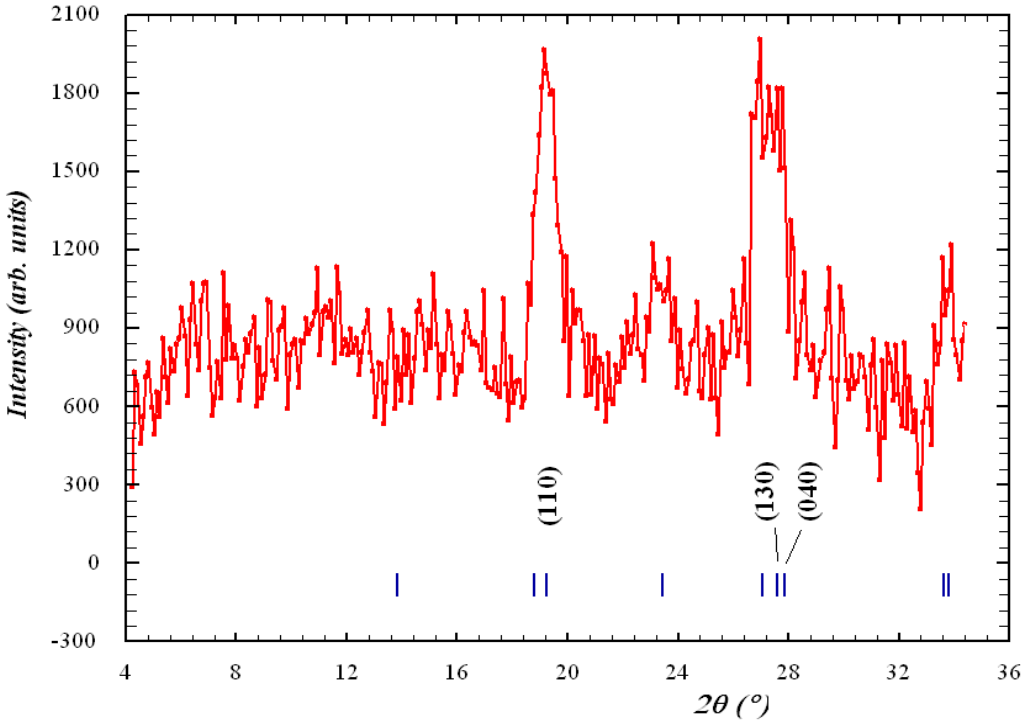

Figure 5.4. The difference between the 220 K and 3.6 K patterns. The labeled Bragg markers indicate some important reflections.

A recent ^{119}Sn Mössbauer spectroscopy study on Sn-doped GdGa (Delyagin et al. 2007) showed that below T_{sr}, which is reported to be 110 K, the Gd magnetic moments form a non-collinear magnetic structure in either the crystallographic ac or ab-plane,

since the Mössbauer measurement was found to be insensitive to the azimuthal angle of the Gd moment direction. According to this study, the Gd magnetic moments at 5 K point in two different directions ($\theta_1 \sim 30^0$ and $\theta_2 \sim 60^0$). Given the poor signal-to-noise ratio of the difference pattern in the present refinement, the possible magnetic structure will be deduced by trial and error. However, it was found necessary to refine the lattice parameters, to account for the lattice contraction as the temperature is lowered.

To begin with, we use the simplest ordering mode of a collinear ferromagnetic structure and also a fixed magnetic moment of 7 μ_B. As discussed earlier, there are eight possible magnetic space groups corresponding to the *Cmcm* space group associated with Gd atoms at the 4c sites, as shown in table 4.2. Simulated patterns were generated for all eight possible magnetic space groups but none gave a good qualitative agreement with the experimental data, which suggests a non-collinear structure. The non-collinear structure itself can be considered as a combination of ferromagnetic and antiferromagnetic structures in which the magnetic moments point in two different directions. Initially, we consider the simplest non-collinear structure which is a non-collinear ferromagnetic structure. For a given eight possible magnetic space groups listed in Table 4.2, we will have 3 simple non-collinear ferromagnetic structures, derived from the combination of the *Cmc'm', Cm'cm'* and *Cm'c'm* magnetic space groups confined to either the crystallographic ab-, ac- or bc-plane, to be compared against the experimental pattern. After several trial and error refinements, the best combination that gave good agreement with the experimental data is a non-collinear ferromagnet in the bc-plane which is the combination of the *Cm'cm'* and *Cm'c'm* magnetic space groups.

Once the possible magnetic structure has been identified, the refinement can

proceed by varying the moment and the canting angles. The best refinement using this non-collinear structure is shown in Figure 5.5. The refined value of the Gd moment is 6.0(2) μ_B, somewhat lower than the 'free-ion' value for the Gd^{3+}, i.e. 7 μ_B. We also find that the Gd magnetic moments are oriented in two different directions, i.e. $\theta_1 = 44(7)^0$ and $\theta_2 = 6(7)^0$, with respect to the c-axis as shown in Figure 5.6 which is in contrast with the result from ^{119}Sn Mössbauer spectroscopy result on Sn-doped GdGa.

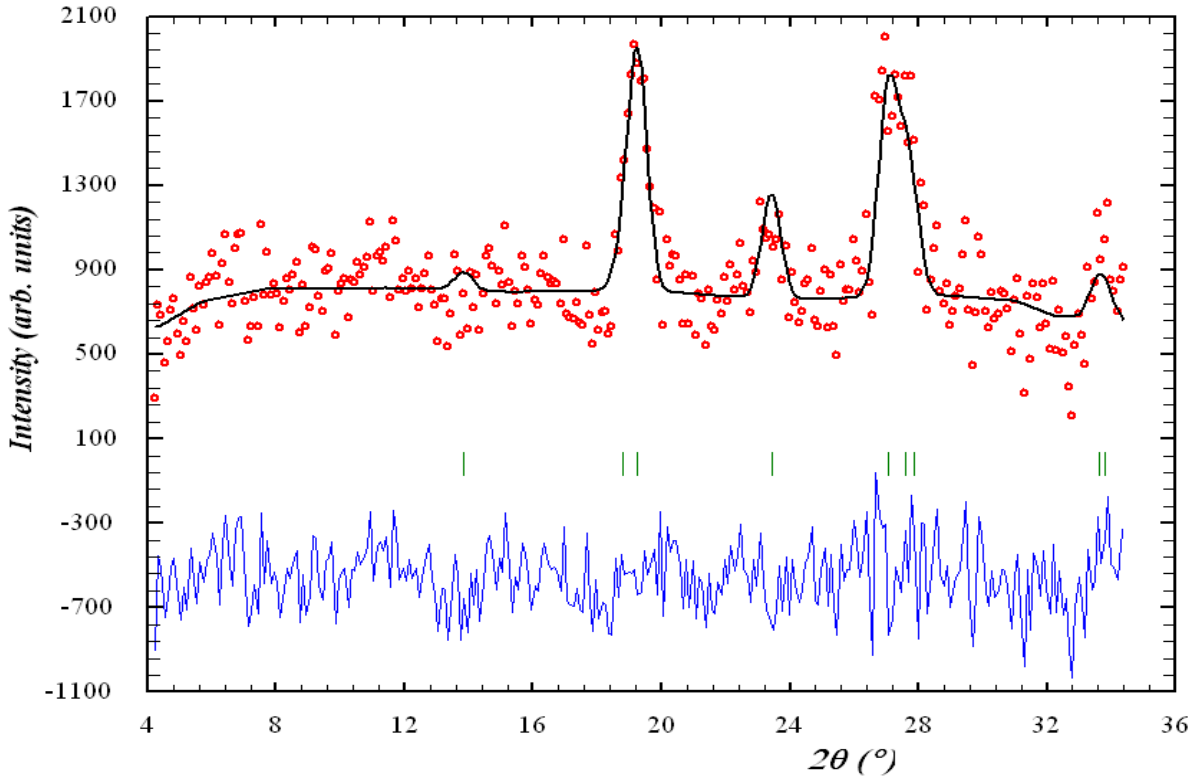

Figure 5.5. The refinement of the difference between the 220 K and 3.6 K patterns for GdGa. The Bragg markers were generated using the $C\bar{1}$ space group.

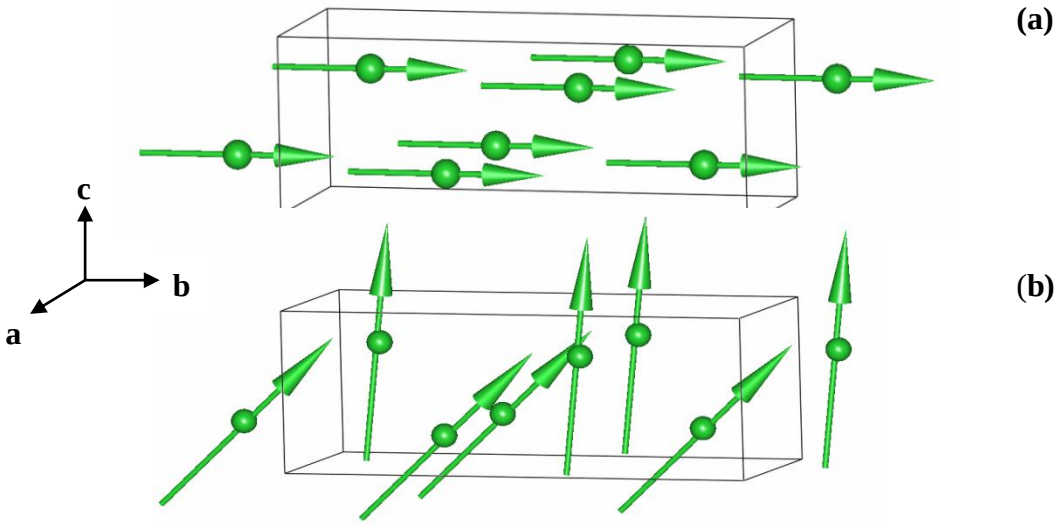

Figure 5.6. Magnetic structure of the Gd sublattice in GdGa above (a) and below (b) the spin reorientation temperature.

Gd^{3+} is an S-state ion which has spherical charge distribution of the 4f electron shell. In such a case, the 4f electron shell distortion due to the crystal field interaction is negligible, thus the direction of the Gd magnetic moments is solely determined by the exchange interaction. The observation of a non-collinear magnetic structure at low temperature as illustrated in Figure 5.7 in which the Gd moments located at z = 0.25 point in a different direction from the Gd moment at z = 0.75, implies that there are two exchange fields acting on a different ab-plane.

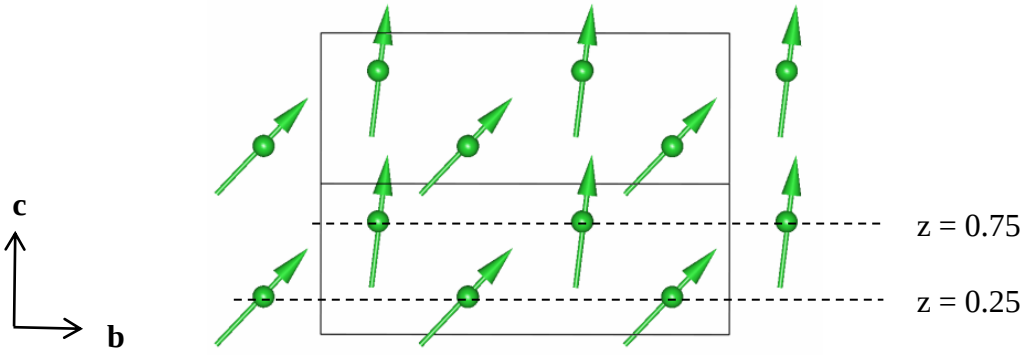

Figure 5.7. Schematic arrangement of the Gd magnetic moments in GdGa at 3.6 K projected onto the bc-plane.

5.4. ^{155}Gd Mössbauer Spectroscopy on GdGa

The ^{155}Gd Mössbauer spectrum of GdGa collected at 5 K is shown in figure 5.8. The spectrum could not be fitted with a single component and thus was fitted using two equal-area subspectra. The values of B_{hf}, $eQVzz$, isomer shift (δ), and the asymmetry parameter (η) for both spectra were kept similar, while the polar angles θ and φ were varied independently for both spectra. The isomer shifts are 0.46 and 0.47 mm/s, relative to the $SmPd_3$ source. The fitting parameters are summarized in Table 5.3.

Due to the *m2m* point symmetry of the Gd site in GdGa, the principal axes of the EFG (XYZ) coincide with the crystallographic axes (abc). Although we cannot identify directly the individual axes, in the following discussion we shall show that we can use the second-order crystal field parameters deduced by Shohata (1977) and Shohata et al. (1974) to determine the axial correspondences.

The EFG at the R sites contains contributions from both the 4f electronic shells of the R^{3+} ion and the surrounding charges (Cadogan & Ryan 2004). Gd^{3+} is an S-state ion, thus the contribution of the 4f shell to the total EFG is zero and the dominant contribution to the total EFG comes from the surrounding lattice charges. It has been shown before

that there are relationships between the EFG tensor components and the second-order crystal field coefficients, in particular $A_{20} \propto V_{ZZ}$ and $A_{22} \propto (V_{xx} - V_{yy})$ (see section 2.4.5). Despite the fact that there is also contribution from the asphericity of the valence-electron charge density to the EFG (Coehoorn et al. 1990), these useful approximations can be used in the following discussion.

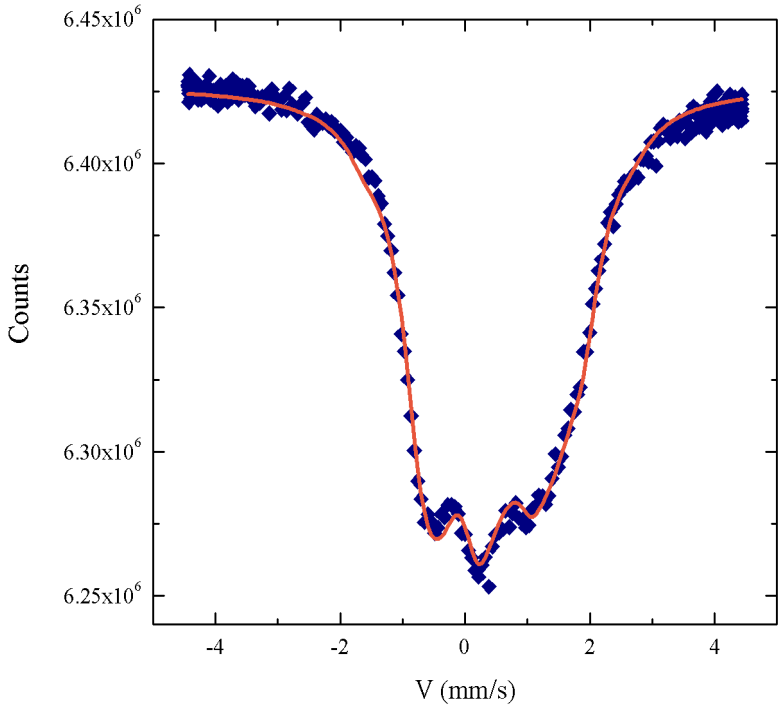

Figure 5.8. ^{155}Gd Mössbauer spectrum of GdGa collected at 5 K.

Table 5.3. The hyperfine parameters of the ^{155}Gd Mössbauer spectrum at 5 K.

	***eQVzz* (mm/s)**	***B*$_{hf}$ (T)**	***η***	***θ* (^{0})**	***φ* (^{0})**	**Area (%)**
Gd$_1$	−1.43(3)	39.8(3)	0.88(1)	49(2)	90	50
Gd$_2$	−1.45(4)	39.5(3)	0.87(1)	0(2)	90	50

The second-order crystal field parameters of RGa were deduced by Shohata (1977) and Shohata et al. (1974) using the crystallographic b-axis as the principal Z-CEF (Crystalline Electric Field) axis with the particular identification of (abc) = (YZX). According to their results (listed in Table 1.3), the average values of A_{20} and A_{22} across the RGa series are −280 K/Å^2 and 464 K/Å^2 respectively. It is conventional to choose the principal axes of the EFG such that

$$|V_{ZZ}| \geq |V_{yy}| \geq |V_{xx}| \tag{5.1}$$

Using the above assumptions, i.e. $A_{20} \propto V_{ZZ}$ and $A_{22} \propto (V_{xx} - V_{yy})$, it can be seen that the average values of the measured A_{20} and A_{22} lead to $|V_{ZZ}| < |V_{xx} - V_{yy}|$, which implies that the b-axis is not the principal Z-EFG axis. Under this condition, one needs to rotate the CEF axes, until the requirement in (5.1) is met, i.e. $|A_{20}| > |A_{22}|$. This can be done using the spin-operator rotational transformations (Rudowicz 1985):

$$\begin{aligned} A_{20}{}' &= \frac{1}{2}(3\cos^2\theta - 1)\,A_{20} + \frac{1}{2}\sin^2\theta\cos 2\varphi\,A_{22} \\ A_{22}{}' &= \frac{3}{2}\sin^2\theta\,A_{20} + \frac{1}{2}(1 + \cos^2\theta)\cos 2\varphi\,A_{22} \end{aligned} \tag{5.2}$$

where the prime signs indicate the rotated parameters. It is straightforward to show that under a rotation of θ = 90^0, φ = 0^0 with respect to the b-axis, the values of $A_{20}{}'$ and $A_{22}{}'$ are 372 K/Å^2 and −188 K/Å^2. Under such rotation, the c-axis is now the principal Z-EFG axis. A further rotation of θ = 0^0, φ = 90^0 with respect to the c-axis yields the $A_{20}{}'$ and $A_{22}{}'$ values of 372 K/Å^2 and 188 K/Å^2, i.e. the condition of $|V_{ZZ}| \geq |V_{yy}| \geq |V_{xx}|$ is fulfilled. Furthermore, under such a rotation we can identify the appropriate EFG axes as (abc) = (XYZ).

The rotated crystal field coefficient $A_{20}{}'$ was also used to check our measured

electric quadrupole coupling constant eQV_{zz} value. As mentioned earlier, we can assume that there is a direct relationship between the diagonal EFG tensor components and the second-order crystal field coefficients. Under this assumption, one often writes the following equation to derive the second-order crystal field coefficient (A_{20}) from *Vzz* (Stewart 1985)

$$A_{20}{}' = -\frac{e}{4} V_{ZZ} / \left(\frac{1-\gamma_\infty}{1-\sigma_2}\right) \tag{5.3}$$

where γ_∞ and σ_2 are the Sternheimer antishielding factor and the lattice shielding factor respectively. The approximate value of $\left(\frac{1-\gamma_\infty}{1-\sigma_2}\right)$ for Gd^{3+} is 212 ± 9, which is reasonably applicable to all Gadolinium intermetallic compounds (Cadogan et al. 2007). Hence, the average value $A_{20}{}'$ of 372 K/Å^2 yields $Vzz = -(2.72 \pm 0.12)\times10^{21}$ V/m^2. Using the electric quadrupole moment of the ^{155}Gd ground state, Q = 1.30 ± 0.02 barns, one obtains a deduced *eQVzz* value of $-(5.66 \pm 0.34)\times10^{-26}$ J which converts to −(1.22 ± 0.08) mm/s (note that for the 86.5 keV Mössbauer transition in ^{155}Gd, 1 mm/s converts to 4.625×10^{-26} J (Cadogan et al. 2007)), in agreement with the average *eQVzz* value from our results, which is − 1.44(5) mm/s.

From Table 5.3, it can be seen the Gd moments point in two different directions, θ_1 = 49(2)^0 and θ_2 = 0(2)^0 with respect to the Z-EFG (the crystallographic c-axis). This result is consistent with our neutron diffraction refinement which shows that the Gd magnetic moments point in two different directions θ_1 = 44(7)^0 and θ_2 = 6(7)^0 with respect to the c-axis on the bc-plane.

5.5. The Interpretation of ^{119}Sn Mössbauer Spectroscopy on Sn-doped GdGa

As discussed earlier, Delyagin et al. (2007) used ^{119}Sn Mössbauer spectroscopy to examine the spin reorientation in Sn-doped GdGa. They showed that the ^{119}Sn spectrum at 5 K can be well fitted using two magnetically split subspectra which led to the suggestion of a non-collinear structure of the Gd sublattice. Although we have shown that we observe a different magnetic structure, we still have one remaining question to answer which is whether the magnetic structure derived from our neutron diffraction refinement at 3.6 K is able to explain the magnetic splitting in the ^{119}Sn Mössbauer spectra.

In order to examine the transferred hyperfine field at the Sn sites in Sn-doped GdGa, we have determined the nearest-neighbour environments of the Sn atoms using the BondStr program embedded in the Fullprof Suite program. Using the lattice parameters and atomic positions from the neutron diffraction refinement at 220 K, we find that each Sn atom (which occupy the Ga sites) is surrounded by seven Gd atoms in the range of distances between 2.70 Å and 3.6 Å.

There are four Sn atoms in Sn-doped GdGa. The nearest-neighbour environment for each Sn atom based on the magnetic structure of GdGa at 3.6 K is illustrated in Figure 5.9. Two of the Sn atoms (labelled as Sn_1) experience a different direction of the net transferred hyperfine field than the other two atoms (Sn_2). This difference in transferred hyperfine field splits these four Sn atoms into two groups, which leads to the two magnetically split subspectra observed by ^{119}Sn Mössbauer spectroscopy.

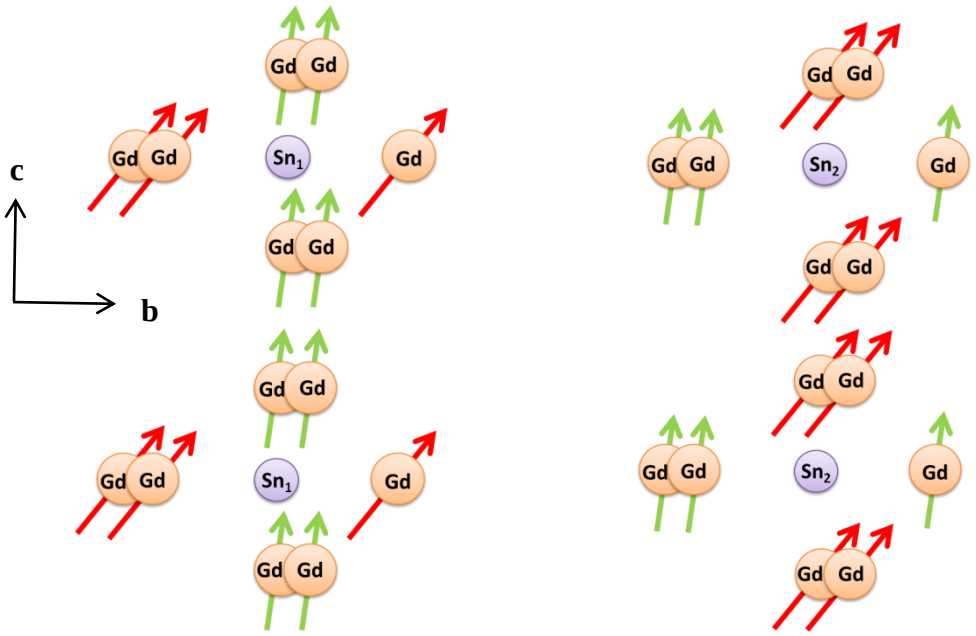

Figure 5.9. Nearest-neighbour environment of the Sn sites in the Sn-doped GdGa. Red and green arrows represent the canting angles of $\theta_{red} = 44^0$ and $\theta_{green} = 6^0$, obtained by neutron diffraction.

5.6. Summary

We have examined the magnetic structure and spin reorientation of GdGa by neutron powder diffraction and ^{155}Gd Mössbauer spectroscopy. At 110 K, the Gd moments are aligned ferromagnetically along the crystallographic b-axis. Upon cooling below the spin reorientation temperature, the Gd moments are canted away from the b-axis. At 3.6 K, we find that the Gd moments form a non-collinear ferromagnetic structure with the Gd magnetic moments pointing in two different directions $\theta_1 = 44(7)^0$ and $\theta_2 = 6(7)^0$ with respect to the c-axis within the bc-plane. This results is consistent with our ^{155}Gd Mössbauer spectroscopy result in which we observe the two Gd moments pointing in two different directions, $\theta_1 = 49(2)^0$ and $\theta_2 = 0(2)^0$ with respect to the Z-EFG axis.

6. Spin Reorientation of ErGa

6.1. Phase Identification

Figure 6.1 shows the x-ray powder diffraction pattern for ErGa. The refinement of this pattern confirmed the formation of the CrB-type *Cmcm* orthorhombic structure with impurities of Er_2O_3 (space group $Ia\bar{3}$) and Er_3Ga_5 (space group *Pnma*) present in the total amount of less than 4 wt%. The lattice parameters are a = 4.2619(2) Å, b = 10.7349(2) Å and c = 4.0320(1) Å. The crystallographic data for the Er and Ga sites are given in Table 6.1.

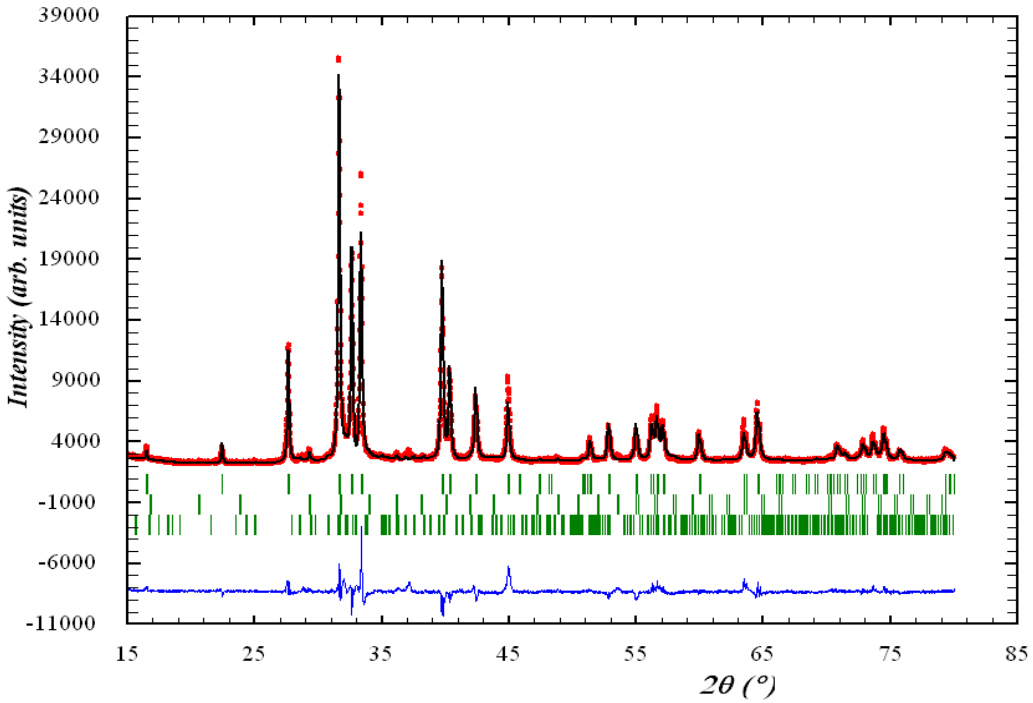

Figure 6.1. X-ray powder diffraction pattern of ErGa collected at room temperature with Cu-Kα radiation. The Bragg markers, from top to bottom, represent ErGa, Er_2O_3 and Er_3Ga_5 respectively.

Table 6.1. Crystallographic data for ErGa.

Atom	x	y	z
Er	0	0.3593(1)	¼
Ga	0	0.0788(2)	¼

6.2. ^{166}Er Mössbauer Spectroscopy

The ^{166}Er Mössbauer spectra on ErGa collected at various temperatures from 35 K to 5 K are shown in Figure 6.2. All spectra were fitted with a single subspectrum with an asymmetry parameter of η = 0. All spectra below 20 K show a well-resolved pentet as expected from the ^{166}Er 2 → 0 transition. The spectra above 20 K are broadened and collapse towards the center with increasing temperature, due to magnetic relaxation effects. It can also be noticed that for the spectra below 17.5 K, the splitting between the 4th and 5th intensity lines (with the 1st intensity line being the left-most line) is increased relative to the splitting between the 1st and 2nd intensity lines. These differences are due to the quadrupole interaction and are related to the increasing value of the quadupole splitting parameter *eQVzz*, which in the case of ^{166}Er Mössbauer with η = 0 and θ = 0 can be written as (Cadogan & Ryan (2004))

$$eQVzz = \frac{4}{3}[(V_5 - V_4) - (V_2 - V_1)] \qquad (6.1)$$

where V_i represent the line positions measured in mm/s. The hyperfine parameters for each temperature are summarized in Table 6.2.

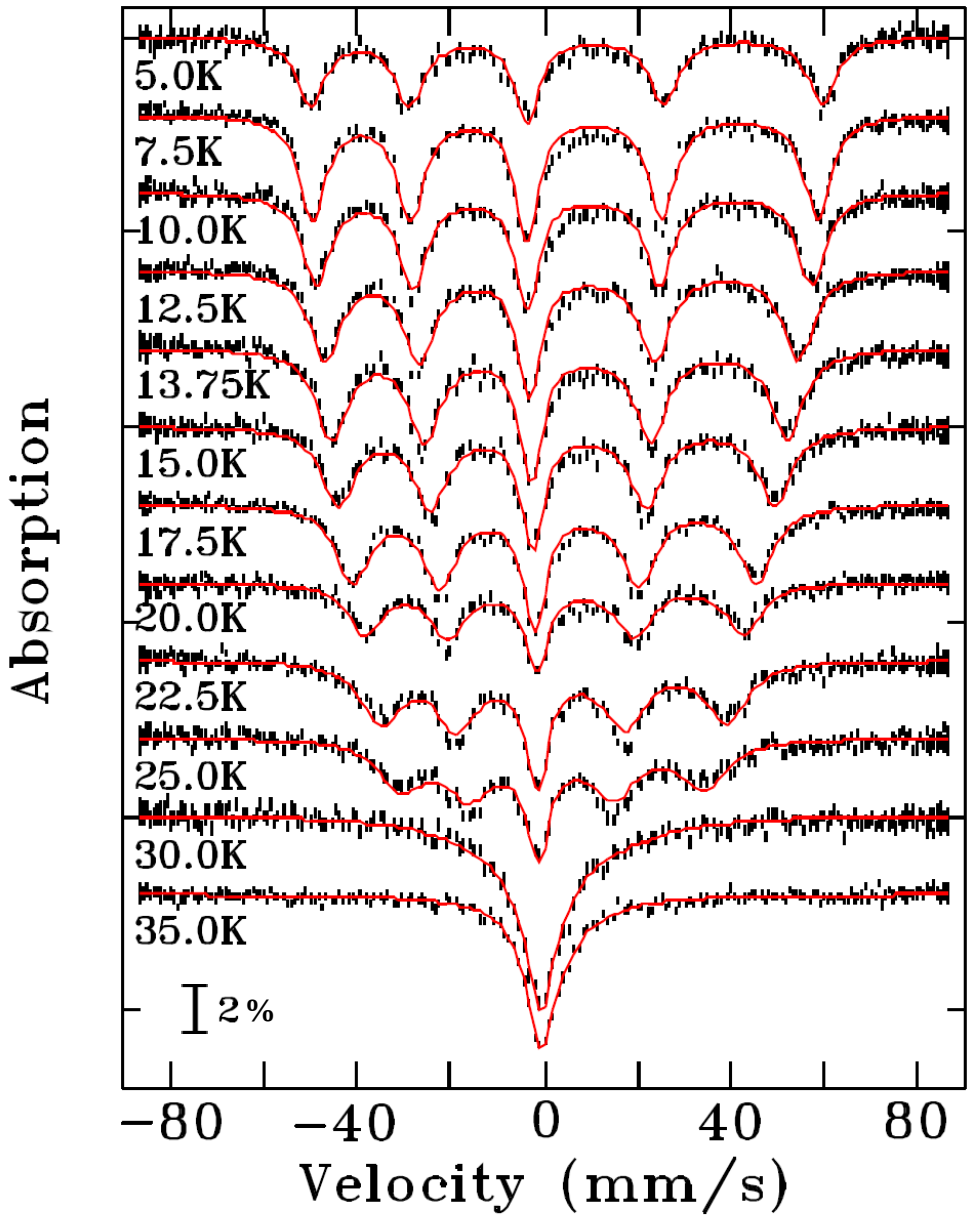

Figure 6.2. ^{166}Er Mössbauer spectra for ErGa obtained at various temperatures

6.2.1. Magnetic Hyperfine Field

The hyperfine field values obtained at various temperatures were used to determine the ordering and spin reorientation temperatures. Assuming both the reduced magnetization, $m = \frac{M(T)}{M(0)}$ and the reduced hyperfine field, $b_{hf} = \frac{B_{hf}(T)}{B_{hf}(0)}$ follow the same temperature dependence, molecular field theory for $T \leq T_c$ shows that the temperature dependence of the hyperfine field can be determined using a Brillouin function $\beta_J(x)$ (Greenwood & Gibb 1971) which is given by

$$B_{hf}(T) = B_{hf}(0)\beta_J(x) \tag{6.2}$$

where

$$\beta_J(x) = \frac{2J+1}{2J}\coth\left(\frac{2J+1}{2J}x\right) - \frac{1}{2J}\coth\left(\frac{1}{2J}x\right);$$
$$x = \frac{3J}{J+1}\frac{b_{hf}}{t}; \quad t = \frac{T}{T_C} \tag{6.3}$$

In the case of the Er^{3+} ion with J = 15/2, equation (6.3) can be written as

$$\beta_{\frac{15}{2}}(x) = \frac{16}{5}\coth\left(\frac{16}{5}x\right) - \frac{16}{5}\coth\left(\frac{16}{5}x\right); \; x = \frac{45}{17}\frac{b_{hf}}{t}; \quad t = \frac{T}{T_C} \tag{6.4}$$

The temperature dependence of the hyperfine field is shown in Figure 6.3. The hyperfine field values above 15 K can be fitted using the Brillouin function $\beta_{\frac{15}{2}}$ following equation (6.2) with $B_{hf}(0)$ = 727(3) T and Tc = 33(1) K (indicated with the solid line). From the figure, we can also see that the change in slope corresponding to the spin reorientation transition Tsr occurs at around 17 K. These values are in agreement with the reported values of Tc = 32(1) K (Fujii et al. 1971, Shohata 1977, Delyagin et al. 2007, Chen et al. 2009) and Tsr ~ 15 K (Delyagin et al. 2007, Chen et al. 2009). Moreover, the

hyperfine field at 5 K is 751.65 ± 1.64 T. Using the moment to field conversion factor of 87.2 ± 1.2 T/μB (Ryan et al. 2003), this hyperfine field value converts to an Er moment of 8.6(2) μB, which is in excellent agreement with the neutron diffraction results of Barbara et al.(1971) i.e. an Er moment of 8.7(5) μB at 4.2 K.

Table 6.2. The ^{166}Er hyperfine parameters of ErGa obtained at various temperatures.

T (K)	***eQVzz* (mm/s)**	**B_{hf} (T)**	**δ (mm/s)**
5.0	16.88 ± 0.36	751.65 ± 1.64	0.57 ± 0.08
7.5	16.43 ± 0.24	741.72 ± 1.06	0.41 ± 0.05
10.0	15.86 ± 0.29	727.70 ± 1.30	0.36 ± 0.06
12.5	13.99 ± 0.28	695.88 ± 1.33	0.30 ± 0.06
13.75	12.33 ± 0.30	670.21 ± 1.49	0.30 ± 0.07
15.0	10.35 ± 0.32	641.88 ± 1.60	0.13 ± 0.07
17.5	8.61 ± 0.29	593.83 ± 1.50	0.14 ± 0.07
20.0	7.76 ± 0.43	557.50 ± 2.30	0.33 ± 0.10
22.5	7.27 ± 0.44	511.78 ± 2.61	0.35 ± 0.11
25.0	6.20 ± 0.60	450.23 ± 3.84	0.30 ± 0.15
30.0	4.50 ± 0.50	313.96 ± 40.38	0.30 ± 0.00
35.0	4.62 ± 0.50	0	0.30 ± 0.00

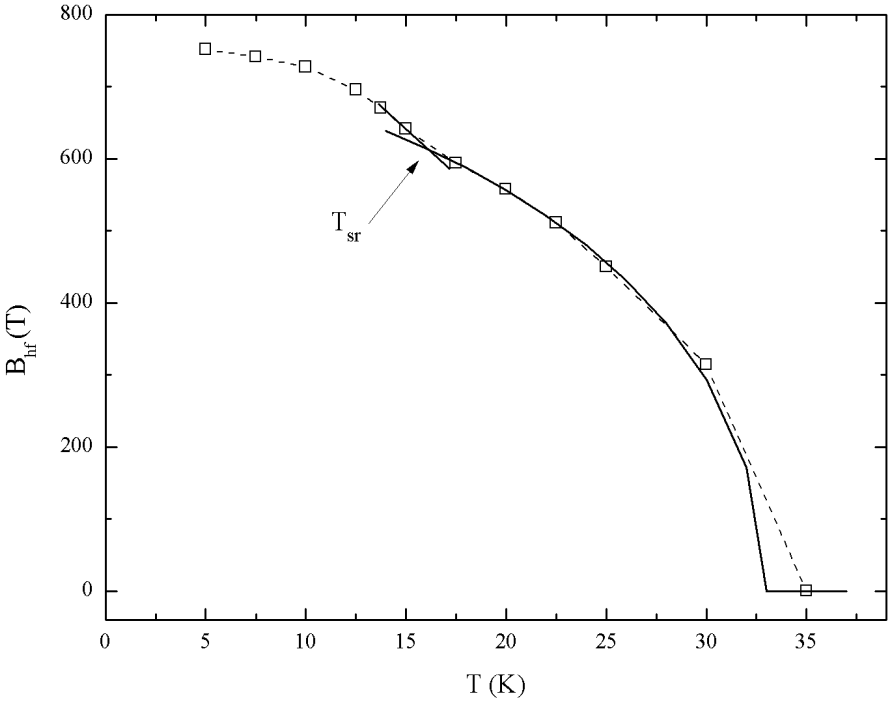

Figure 6.3. The temperature dependence of the ^{166}Er hyperfine field. The solid line represents the Brillouin function $\beta_{\frac{15}{2}}$. The dashed curve is a guide to the eye.

6.2.2. Electric Quadrupole Interaction

The quadrupole splitting parameter *eQVzz* shows a strong temperature dependence as seen in Figure 6.4. In contrast with ^{155}Gd where the total EFG comes from the surrounding lattice charges, the contribution to the total EFG at the ^{166}Er nucleus mostly comes from the crystal field distortion of the 4f shell, hence it has a temperature-dependence. The sudden increase in *eQVzz* by about ~ 5 mm/s between 17 K and 10 K is related to the spin reorientation transition. At 4 K, the *eQVzz* value is 16.9(4) mm/s, close to the 'free-ion' value of 16.3(7) mm/s (Bleaney 1979), although it is slightly higher, indicating a lattice contribution to the total EFG.

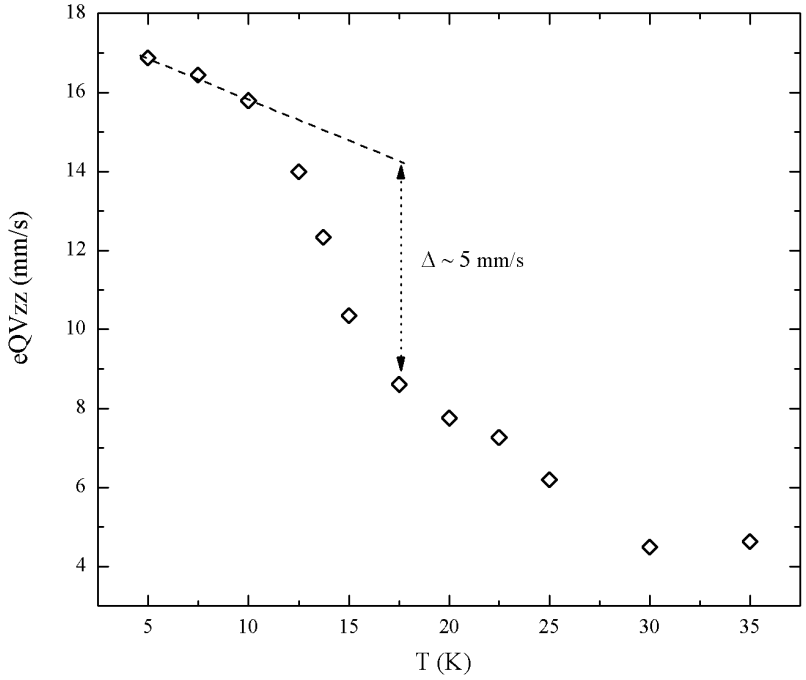

Figure 6.4. The temperature dependence of the ^{166}Er quadrupole splitting parameter *eQVzz*. The sudden increase about 5 mm/s between 17 and 10 K is clear.

The total EFG at the ^{166}Er nucleus in the presence of hyperfine field can be written as (Cadogan et al. 2003)

$$eQVzz = eQVzz^{4f} + \frac{eQVzz^{latt}}{2}(3\cos^2\theta - 1) \tag{6.5}$$

assuming the asymmetry parameter η = 0 from the Mössbauer fitting. The angle θ represents the direction of the hyperfine field with respect to the principal Z-EFG axis. The $eQVzz^{latt}$ for ErGa can be estimated from the purely lattice contribution to the total EFG in GdGa, using the relation

$$eQVzz^{latt}(Er) = eQVzz^{latt}(Gd) \times \frac{Q(Er)}{Q(Gd)} \times \frac{E_\gamma(Gd)}{E_\gamma(Er)} \tag{6.6}$$

where $Q(Er)$ and $Q(Gd)$ are the electric quadrupole moments of ^{166}Er and ^{155}Gd, equal to −1.9(4) and 1.30(2) barns respectively. $E_\gamma(Gd)$ and $E_\gamma(Er)$ are the transition energies

for ^{155}Gd and ^{166}Er equal to 86.546 and 80.557 keV, respectively. Using our average *eQVzz* value of $-1.44(5)$ mm/s for ^{155}Gd in GdGa, one obtains an $eQVzz^{latt}(Er)$ of 2.26(60) mm/s. Moreover, the angular term in (6.5) has minimum and maximum values of -1 (for θ = 90^0) and +2 (for θ = 0^0), hence we expect a maximum change of the $eQVzz^{latt}$ of 3.39 mm/s due to the lattice contribution only. As mentioned earlier, we observed a sudden increase in *eQVzz* of about 5 mm/s, indicating that this change cannot be attributed solely to the change in $eQVzz^{latt}$, but also the change in $eQVzz^{4f}$ due to the crystal field interaction. The dominant contribution to the Vzz^{4f} comes from the temperature-dependence of $\langle O_{20} \rangle$ where $O_{20} = 3{J_z}^2 - J(J+1)$. This term is essentially the Boltzmann average of the Stevens operator over the thermally populated crystal field levels. For the *m2m* point symmetry of the Er site in ErGa, the total energy of the system can be described by a Hamiltonian containing the interaction of the Er^{3+} ion with the crystal field and the exchange field, which can be written as

$$\begin{aligned} H_{Total} &= H_{CF} + H_{exch} \\ &= B_{20}O_{20} + B_{22}O_{22} + B_{40}O_{40} + B_{42}O_{42} + B_{44}O_{44} + \\ &\quad B_{60}O_{60} + B_{62}O_{62} + B_{64}O_{64} + B_{66}O_{66} - g_J\mu_B\vec{J}\cdot\vec{B}_{exch} \end{aligned} \tag{6.7}$$

where g_J is the Landé g-factor of Er^{3+} ion, equal to 1.2, and the $\vec{B}_{exch}$ is the exchange field acting at the Er site. The diagonalization of the Hamiltonian in (6.7) can be used to calculate the expectation value of $\langle J_z \rangle$ via

$$\langle J_z \rangle = \sum_{\Gamma} n_\Gamma \langle \Gamma \mid J_z \mid \Gamma \rangle \tag{6.8}$$

where

$$n_\Gamma = \frac{\exp(\frac{-E_\Gamma}{kT})}{Z} \quad ; \quad Z = \sum_\Gamma \exp(\frac{-E_\Gamma}{kT}) \tag{6.9}$$

Z is the partition function and $|\Gamma\rangle$ is the eigenstate corresponding to the eigenvalue E_Γ of the Hamiltonian in (6.7). It can be seen that the expectation value of $\langle J_z \rangle$ depends on the crystal field parameters B_{20} ... B_{66}. Thus, we can say that the sudden increase in *eQVzz* is not only due to the change in the Er moment direction with respect to the principal Z-EFG axis, but also the change in the expectation value of $\langle J_z \rangle$ because of the crystal field interaction. Unfortunately, we could not determine the Er moment direction solely from this ^{166}Er Mössbauer measurement, and neutron powder diffraction measurement at various temperatures are planned in the near future to give a definitive determination. To this end, we have already prepared a large sample of ErGa sufficient for the neutron diffraction experiments.

6.3. Summary

We have used ^{166}Er Mössbauer spectroscopy to study the spin reorientation in ErGa. Both the quadrupole splitting parameter and the hyperfine field show sudden increases at around 17 K, which are related to the spin reorientation transition. From the hyperfine field value at 5 K, we are able to deduce an Er moment of 8.6(2) μ_B which is in excellent agreement with the previous neutron diffraction result of 8.7(5) μ_B (Barbara et al. 1971).

7. General Conclusions and Suggestions for Future Work

7.1. General Conclusions

The magnetic structures and spin reorientations of the RGa (R = Gd, Dy, Ho and Er) intermetallic compounds have been studied using neutron powder diffraction and rare earth Mössbauer spectroscopy. The magnetic structure determination was performed using a symmetry analysis based on the magnetic space groups and all neutron diffraction data were refined using the Rietveld method.

Neutron diffraction data on DyGa and HoGa shows that both the Dy and Ho sublattices order ferromagnetically along the c-axis below their Curie temperatures. At 3 K, the Dy moment is 9.6(4) μ_B. However, no spin reorientation was observed in this compound. In contrast, neutron powder diffraction data on HoGa at 3 K shows that the Ho moments cant away from the c-axis towards the ab-plane. The refined magnetic moment for the Ho ion is 8.8(2) μ_B at 3 K, and its direction is defined by the polar angles of $\theta = 30(2)^0$ and $\varphi = 49(4)^0$ relative to the crystallographic c-axis. This behavior is driven by competition between the different crystal field orders, with the higher order (6^{th}) term becoming significant as the temperature is lowered.

Neutron diffraction on GdGa reveals that the Gd sublattice orders ferromagnetically along the b-axis just below the Curie temperature. To our knowledge, this is the first clear determination of the Gd moment's direction in GdGa. Upon cooling below the Curie temperature, the Gd magnetic moments cant away from the b-axis. At 3.6 K, the refined Gd moment is 6.0(2) μ_B and the Gd moments form a non-collinear ferromagnetic structure with the Gd magnetic moments pointing in two different

directions $\theta_1 = 44(7)^0$ and $\theta_2 = 6(7)^0$ with respect to the c-axis within the bc-plane. ^{155}Gd Mössbauer spectroscopy on GdGa confirms our neutron diffraction refinement, in which we observe canting angles of $\theta_1 = 49(2)^0$ and $\theta_2 = 0(2)^0$ with respect to the Z-EFG axis at 5 K. It has also been shown that the individual EFG axes are (XYZ) = (abc), based on average value of the second-order crystal field parameters obtained by Shohata et al. (1977).

The spin reorientation in ErGa has been studied using ^{166}Er Mössbauer spectroscopy. The quadrupole splitting parameter value (*eQVzz*) shows a strong temperature-dependence. Sudden increases in both the quadrupole splitting parameter and the hyperfine field are observed at 17 K and are related to the reorientation of the Er moments. It has been shown that the sudden increase in *eQVzz* of ~ 5 mm/s cannot be attributed solely to the change in the Er moment direction with respect to the principal Z-EFG axis, but also encompasses the change in the expectation value of $\langle O_{20} \rangle$ due to the crystal field interaction. Based on the hyperfine field value at 5 K, we deduce an Er moment of 8.6(2) μ_B which is in excellent agreement with the previous neutron diffraction result of Barbara et al. (1971), i.e. an Er moment of 8.7(5) μ_B at 4.2 K.

7.2. Suggestions for Future Work

a. Neutron powder diffraction measurement on ErGa should be carried out at a number of temperatures (above T_c, just below T_c, above T_{sr}, below T_{sr}) to determine the magnetic structures before and after spin reorientation transition. The original data, obtained at 4 K (Barbara et al. 1971) only show the low temperature magnetic structure, and our analysis of the existing magnetometry

work (Shohata 1977) suggests that the spin-reorientation in ErGa at 17 K may in fact be a spin-flip from the b-axis to the a-axis

b. It would be interesting to do ^{155}Gd and ^{157}Gd NMR spectroscopy in GdGa, and compare the results with the hyperfine parameters obtained from the ^{155}Gd Mössbauer spectroscopy at 5 K.

c. Until now, there is no report regarding the magnetic structure of TmGa. It would be interesting to investigate its magnetic structure using both neutron powder diffraction and ^{169}Tm Mössbauer spectroscopy.

References

International Tables for Crystallography Volume A: Space-Group Symmetry. (Springer, 2005).

Aleonard, R., Boutron, P. and Bloch, D., *Journal of Physics and Chemistry of Solids* **30** (9), 2277-2285 (1969).

Baenziger, N. C. and Moriarty, J. L., Jnr, *Acta Crystallographica* **14** (9), 946-947 (1961).

Barbara, B., Becle, C., Nguyen, N. N. and Siaud, E., *Conference Digest no. 3, Rare earth and Actinides, Institute of Physics, Durham* (1971) pp. 219-221.

Barbara, B., Gignoux, D. and Vettier, C., *Lectures on Modern Magnetism*. (Science Press, Beijing, 1988).

Bleaney, B., in *Magnetic Properties of Rare Earth Metals*, edited by R. J. Elliott (Plenum, London, 1979).

Blume, M. and Tjon, J. A., *Physical Review* **165** (2), 446-456 (1968).

Buschow, K. H. J., *Reports on Progress in Physics* **42** (8), 1373-1477 (1979).

Buschow, K. H. J. and De Boer, F. R., *Physics of Magnetism and Magnetic Materials*. (Kluwer Academic, New York, 2003).

Cable, J. W., Koehler, W. C. and Wollan, E. O., *Physical Review* **136** (1A), A240-A242 (1964).

Cadogan, J. M., Ryan, D. H., Moze, O., Suharyana and Hofmann, M., *Journal of Physics: Condensed Matter* **15** (10), 1757-1771 (2003).

Cadogan, J. M. and Ryan, D. H., in *Handbook of Applied Solid State Spectroscopy*, edited by D. R. Vij (Springer US, 2006), pp. 201-256.

Cadogan, J. M. and Ryan, D. H., *Hyperfine Interactions* **153** (1), 25-41 (2004).

Cadogan, J. M., Ryan, D. H. and Cashion, J. D., *Journal of Physics: Condensed Matter* **19** (21), 216204 (2007).

Cadogan, J. M., Ryan, D. H., Napoletano, M., Riani, P. and Cranswick, L. M. D., *Journal of Physics: Condensed Matter* **21** (12), 124201 (2009).

Cadogan, J. M., Ryan, D. H. and Swainson, I. P., *Journal of Physics: Condensed Matter* **12** (42), 8963-8971 (2000).

Cagliotti, G., Paoletti, A. and Ricci, F. P., *Nuclear Instruments and Methods* **3,** 223-228 (1958).

Chatterji, T., in *Neutron Scattering from Magnetic Materials*, edited by T. Chatterji (Elsevier, 2006).

Chen, J., Shen, B. G., Dong, Q. Y., Hu, F. X. and Sun, J. R., *Applied Physics Letters* **95** (13), 132504 (2009).

Chen, J., Shen, B. G., Dong, Q. Y. and Sun, J. R., *Solid State Communications* **150** (3-4), 157-159 (2010).

Chipaux, R., *Computer Physics Communications* **60** (3), 405-415 (1990).

Coehoorn, R., Buschow, K. H. J., Dirken, M. W. and Thiel, R. C., *Physical Review B* **42** (7), 4645-4655 (1990).

Delyagin, N. N., Krylov, V. and Rozantsev, I., *Journal of Magnetism and Magnetic Materials* **308** (1), 74-79 (2007).

Dwiggins, C., Jnr, *Acta Crystallographica Section A* **31** (1), 146-148 (1975).

Dwight, A. E., Downey, J. W. and Conner, R. A., Jnr, *Acta Crystallographica* **23** (5), 860-862 (1967).

Elliott, R. J. and Stevens, K. W. H., *Proceedings of the Royal Society A* **218**, 553-566 (1953).

Fujii, H., Shohata, N., Okamoto, T. and Tatsumoto, E., *Journal of the Physical Society of Japan* **31**, 1592 (1971).

Gignoux, D. and Schmitt, D., in *Handbook of Magnetic Materials*, edited by K. H. J. Buschow (Elsevier, 1997), Vol. 10, pp. 239-413.

Gonser, U., *Mössbauer Spectroscopy*. (Springer-Verlag, New York, 1975).

Greenwood, N. N. and Gibb, T. C., *Mössbauer Spectroscopy*. (Chapman and Hall Ltd, London, 1971).

Hutchings, M. T., in *Solid State Physics*, edited by S. Frederick and T. David (Academic Press, 1964), Vol. 16, pp. 227-273.

Iraldi, R., Nguyen, V. N., Rossat-Mignod, J. and Tcheou, F., *Solid State Communications*

15 (9), 1543-1546 (1974).

Kuz'min, M. D. and Tishin, A. M., in *Handbook of Magnetic Materials*, edited by K. H. J. Buschow (Elsevier, 2007), Vol. 17, pp. 149-233.

Leithe-Jasper, A. and Hiebl, K., *Physica Status Solidi A* **155**, 223-231 (1996).

Liss, K.-D., Hunter, B., Hagen, M., Noakes, T. and Kennedy, S., *Physica B: Condensed Matter* **385-386, Part 2** (0), 1010-1012 (2006).

Lobanov, N. N. and Alte da Veiga, L. (1998). 6th European Powder Diffraction Conference**:** Abstract P12-16.

Lynn, J. E. and Seeger, P. A., *Atomic Data and Nuclear Data Tables* **44**, 191-207 (1990).

Maslen, E. N., *International Tables for Crystallography Vol. C*. (2004).

McCusker, L. B., Von Dreele, R. B., Cox, D. E., Louer, D. and Scardi, P., *Journal of Applied Crystallography* **32** (1), 36-50 (1999).

Mössbauer, R. L., *Z. Physik* **151**, 124-143 (1958).

Nesterov, V. I., Reiman, S. I. and Rozantsev, I. N., *Soviet Physics, Solid State* **34**, 671-673 (1992).

NRC-CNBC (2009). C2: Automation of sample alignment. from http://www.nrc-cnrc.gc.ca/eng/programs/cnbc/neutron-techniques/c2.html.

Prandl, W., in *Neutron Diffraction*, edited by H. Dachs (Springer, Berlin, 1978).

Reis, R. D. d., Silva, L. M. d., Santos, A. O. d., Medina, A. M. N., Cardoso, L. P. and Gandra, F. G., *Journal of Physics: Condensed Matter* **22** (48), 486002 (2010).

Rietveld, H., *Journal of Applied Crystallography* **2** (2), 65-71 (1969).

Rodríguez-Carvajal, J., *Physica B: Condensed Matter* **192** (1-2), 55-69 (1993).

Roisnel, T. and Rodríguez-Carvajal, J., *Materials Science Forum* **378-381**, 118-123 (2001).

Rossat-Mignod, J., in *Methods of Experimental Physics Part C*, edited by K. Skold and D. L. Price (Academic Press, Inc., 1987), Vol. 23, pp. 69-157.

Rudowicz, C., *Journal of Physics C: Solid State Physics* **18** (7), 1415-1430 (1985).

Ryan, D. H. and Cranswick, L. M. D., *Journal of Applied Crystallography* **41** (1), 198-205 (2008).

Ryan, D. H. (2011). from http://www.physics.mcgill.ca/~dominic/.

Ryan, D. H., Cadogan, J. M. and Gagnon, R., *Physical Review B* **68** (1), 014413 (2003).

Shohata, N., *Journal of the Physical Society of Japan* **42**, 1873-1880 (1977).

Shohata, N., Fujii, H. and Okamoto, T., *Journal of the Physical Society of Japan* **37**, 567 (1974).

Squires, G. L., *Introduction to The Theory of Thermal Neutron Scattering*. (Cambridge University Press, Cambridge, 1978).

Stevens, K. W. H., *Proceedings of the Physical Society. Section A* **65** (3), 209-215 (1952).

Stewart, G. A., *Hyperfine Interactions* **23** (1), 1-16 (1985).

Stewart, G. A., Harker, S. J., Strecker, M. and Wortmann, G., *Physical Review B* **61** (9), 6220-6226 (2000).

Toby, B. H., *Journal of Applied Crystallography* **34**, 210–221 (2001).

von Dreele, R. B. and Larson, A. C., *Los Alamos National Laboratory LAUR Report* (unpublished), 86–748 (2004).

Wallace, W. E., *Rare Earth Intermetallics*. (Academic Press, New York, 1973).

Young, R. A., *The Rietveld Method*. (Oxford University Press, New York, 1993).

Zhang, J. Y., Luo, J., Li, J. B., Liang, J. K., Wang, Y. C., Ji, L. N., Liu, Y. H. and Rao, G. H., *Journal of Alloys and Compounds* **469** (1-2), 15-19 (2009).

Appendix A

The comparison of the normalized 3.6 K pattern of GdGa taken at different times. The patterns are plotted versus Q to show the effect of wavelength on the resolution. The artefact mentioned in the discussion is indicated with the asterisk.